Bioresource Technology 449 (2026) 134403

Contents lists available at ScienceDirect

Bioresource Technology

journal homepage: www.elsevier.com/locate/biortech

Nitrogen-rich biochar electrodes from urban green waste for microbial CO_2 electroreduction in bioelectrochemical systems

Khair Un Nisa [a], Beatrice Ricciardi [a], Williane da Silva Freitas [a], Manuela Montalto [a], Alessandra D'Epifanio [a], Pietro Mele [b], Lorenzo Bartolucci [b], Fabrizio Arciprete [c], Gabriele Soggia [d], Fabrizio Adani [d], Niccolò Forin [e], Andrea Squartini [e], Barbara Mecheri [a,*]

[a] Department of Chemical Science and Technologies, University of Rome Tor Vergata, Via Della Ricerca Scientifica 1, 00133 Rome, Italy
[b] Department of Industrial Engineering, University of Rome Tor Vergata, Via del Politecnico 1, Rome 00133, Italy
[c] Department of Physics, University of Rome Tor Vergata, Via Della Ricerca Scientifica 1, 00133 Rome, Italy
[d] Gruppo Ricicla Lab., Department of Agricultural and Environmental Sciences, University of Milan, Via Celoria 2, 20133, Italy
[e] Department of Agronomy, Food, Natural Resources, Animals and Environment, DAFNAE, University of Padova, Viale Dell'Università 16, 35020 Legnaro, Italy

HIGHLIGHTS

- One-pot pyrolysis–activation of urban green waste yields *N*-rich biochar electrodes.
- Optimized porosity and *N*-functionalities enhance ORR, HER, and CO_2 electroreduction.
- Biochar-based cathodes boost current density and microbial CO_2 fixation in MES.
- Developed electrodes advance CO_2 electroreduction in bioelectrochemical systems.

GRAPHICAL ABSTRACT

ARTICLE INFO

Keywords:
Bioelectrochemical systems
Microbial electrosynthesis
CO_2 electroreduction
Sustainable biomass conversion
Engineered biochar electrodes, waste-to-resource valorization

ABSTRACT

Bioelectrochemical systems (BES), including microbial electrosynthesis (MES), represent a sustainable route for carbon recycling through CO_2 electroreduction driven by electroactive microorganisms. However, their performance is often limited by sluggish cathodic reactions and the high cost of efficient electrodes. Nitrogen-rich biochar obtained from biomass provides a low-cost, conductive, and porous matrix with abundant active sites, making it suitable for enhancing electron transfer and catalytic activity.

In this study, two biomass precursors with distinct nitrogen contents—hazelnut shells (HZS, low N) and urban green waste (UGW, high N)—were screened for biochar electrode production. Physicochemical and electrochemical analyses identified UGW as the most promising feedstock. The pyrolysis and activation processes were optimized by tuning temperature, residence time, and activation strategies (KOH and CO_2 flow) to maximize nitrogen retention up to 2.90 wt% and porosity in the 450–613 m^2g^{-1} range.

The resulting UGW-derived biochar exhibited partially graphitized, nitrogen-enriched structures with high activity for oxygen reduction reaction (ORR), hydrogen evolution reaction (HER), and CO_2 electroreduction under near-neutral conditions. When used as cathodes in MES cells, these materials promoted enhanced CO_2 fixation and supported microbial communities dominated by Clostridiaceae and Eubacteriaceae, achieving average current densities of around 0.20 mA cm^{-2} over 21-day chronoamperometric tests, consistently higher

* Corresponding author.
E-mail address: barbara.mecheri@uniroma2.it (B. Mecheri).

https://doi.org/10.1016/j.biortech.2026.134403
Received 9 December 2025; Received in revised form 17 February 2026; Accepted 9 March 2026
Available online 10 March 2026

than those of the biochar-free control. These results highlight UGW-derived nitrogen-rich biochars as sustainable cathode materials enabling efficient CO_2 electroreduction and MES for circular carbon utilization.

1. Introduction

Bioelectrochemical systems (BES), such as microbial fuel cells and microbial electrosynthesis (MES) systems, are emerging technologies for coupling waste treatment with energy recovery or the production of value-added compounds (Rinaldi et al., 2008; Caizán-Juanarena et al., 2020; Palanisamy et al., 2019; Li et al., 2017; Bian et al., 2020). MES enables the electrochemical reduction of CO_2 into multi-carbon compounds (*i.e.*, organic acids, alcohols, and volatile fatty acids) mediated by electro-autotrophic microorganisms that accept electrons directly from the cathode or indirectly via hydrogen, allowing efficient product formation under low electrical energy input (Bakonyi et al., 2023; Li et al., 2024).

Electrode materials are central to both electron transfer efficiency and overall process sustainability (Li et al., 2017; Santoro et al., 2022; Li et al., 2025; Zhang et al., 2025; Aysla Costa De Oliveira et al., 2020; Zago et al., 2024). Biochar, a carbon-rich material obtained from biomass pyrolysis, has gained attention as a sustainable, low-cost alternative due to its renewable origin, conductivity, porosity, and environmental compatibility (Li et al., 2021; Li et al., 2025; Wang et al., 2024; Ramírez et al., 2024; Pepè Sciarria et al., 2020; Yu et al., 2024; Wang et al., 2024; Saisuwan et al., 2025; Chen et al., 2025). Its electrochemical performance depends strongly on feedstock type and pyrolysis conditions, which govern surface area, pore structure, conductivity, and surface chemistry (Cancelliere et al., 2025; Goglio et al., 2025; Hassan et al., 2020; Ghodake et al., 2021; Ji et al., 2022; Ferraro et al., 2024; Wang et al., 2025; Chen et al., 2024; Zhang et al., 2025).

Recent studies have increasingly explored biochar-based electrodes specifically for MES, highlighting their potential to enhance both electrochemical performance and biocompatibility (Antic Gorrazzi et al., 2023; Li et al., 2023; Hassan et al., 2019). Owing to their hierarchical porosity, surface functional groups, and carbonaceous structure, biochars promote microbial attachment, biofilm development, and efficient electron transfer at the bio–electrode interface, resulting in an overall performance comparable to or exceeding that of conventional carbon materials (Park et al., 2025; Soggia et al., 2024). In particular, enhanced current densities and higher faradaic efficiencies have been associated with high specific surface area, graphitic domains, and heteroatom functionalities, which facilitate charge transport and microbial–electrode interactions (Hassan et al., 2019; Langsdorf et al., 2024). More advanced electrode designs have further integrated biochar with functional modifiers (e.g., nitrogen doping, metal-based components, or conductive coatings), demonstrating that tailored surface chemistry and architecture can substantially improve catalytic activity and microbial electrosynthesis rates. At the same time, several studies underline that the benefits of such modifications depend strongly on the intrinsic properties of the pristine biochar and on how these properties translate into performance under realistic MES operating conditions (Park et al., 2025; Soggia et al., 2024). Consequently, understanding and controlling the structural and chemical features of biochar through synthesis and post-treatment strategies remains a critical aspect for the rational design of efficient MES electrodes. Activation, either chemical (e.g., KOH) or physical (e.g., CO_2 or steam), enhances porosity and accessibility of active sites, improving mass transport and electron transfer (Venkatachalam et al., 2023; Patra et al., 2021; Panwar and Pawar, 2022; Guo et al., 2009; Sajjadi et al., 2019). Chemical activation produces a higher surface area, mesoporosity, and oxygen-containing groups; however, it involves harsh reagents and presents challenges for scale-up (Venkatachalam et al., 2023; Patra et al., 2021). Physical activation generates micropores that can expand into *meso*- and macropores while preserving structural integrity, offering a more sustainable and scalable route (Panwar and Pawar, 2022; Guo et al., 2009; Sajjadi et al., 2019). The ability to develop a hierarchy of porosity can effectively guide the design of electrocatalysts across different structural scales (Chacón et al., 2020; Kumar Mishra et al., 2023; Leng et al., 2021).

Nitrogen functionalization further enhances biochar performance in electrochemical applications by introducing pyridinic-, pyrrolic-, and graphitic-N groups, which serve as active sites for the adsorption of gases, metals, and organics through Lewis acid-base interactions, hydrogen bonding, and electrostatic forces (Leng et al., 2020; Li et al., 2023; Huang et al., 2023; Choi et al., 2025; Jiang et al., 2025; Zhang et al., 2023). *N*-doping enhances electrocatalytic activity for ORR, oxygen evolution reaction (OER), HER, and CO_2 reduction, increasing the effectiveness of carbon-based materials as electrocatalysts, and can improve energy storage properties such as capacitance and wettability (Zhong et al., 2019; Tan et al., 2025; Fu et al., 2023; Escudero-Curiel et al., 2025; S. Dongre et al., 2025; Chen et al., 2025; Sangprasert et al., 2022; Yao et al., 2021) Nitrogen can be incorporated via wet impregnation of *N*-rich precursors or post-treatments, such as annealing under ammonia (Leng et al., 2020; Mecheri et al., 2018; W. da S. Freitas et al., 2021; Lai et al., 2025; Xue et al., 2025), although these add steps and increase cost. Self-doping with nitrogen-rich feedstocks enables intrinsic nitrogen incorporation during pyrolysis, with biomass type significantly affecting retention. Biochars derived from agricultural residues and urban green waste typically exhibit higher nitrogen levels than those from the organic fraction of municipal solid waste (Xue et al., 2024; Ruan et al., 2025; Zhang et al., 2025; Singh et al., 2022; Johnravindar et al., 2021; Huang et al., 2021; Bartolucci et al., 2023).

Graphitization is another key factor influencing conductivity, stability, and durability. High-temperature treatments enhance graphitic domains, addressing the low conductivity of amorphous biochars, but require careful optimization to balance porosity, surface chemistry, and process sustainability (Zhang et al., 2023; Huang et al., 2021; Chen et al., 2025; Schmies et al., 2023; Yameen et al., 2024).

In this study, we developed a pyrolysis–activation approach to produce nitrogen-rich biochar from urban green waste, maximizing intrinsic N retention while enhancing porosity, surface area, and graphitization. The resulting materials were evaluated as cathodes in microbial electrosynthesis systems for the electroreduction of CO_2 into multi-carbon compounds. Electrochemical characterization and microbial community analysis at the cathode were performed to assess the capability of biochar electrodes to support electron transfer and microbial growth in MES, highlighting their potential as sustainable bio-derived materials for bioelectrochemical applications.

2. Experimental Section

2.1. Materials

Hazelnut shells (HZS) were supplied from Assofrutti S.r.L. (Viterbo, Italy) Urban green waste (UGW) was collected from the autumn garden cuttings in the green areas of the Science Macroarea at the University of Rome Tor Vergata. Before being subjected to pyrolysis, UGW were dried in a static oven for 12 h at 70 °C, while HZS did not undergo any further drying. All the feedstocks were then sieved to obtain a particle size between 300–500 μm. Melamine (98 %) and imidazole (98 %) were supplied by Sigma-Aldrich. Nafion solution (5 wt% in lower aliphatic alcohols and water, 15–20 %), 2-propanol (99.9 %), Polytetrafluoroethylene (PTFE, 60 wt% dispersion in H_2O) were purchased from Sigma–Aldrich. Carbon Vulcan XC 72R was supplied by the CABOT Corporation (Boston, MA, USA). Commercial carbon cloth (CeTech

Carbon Cloth without MPL − W0S1011, Fuel Cell Store) was used for electrode preparation, and Millipore water (18.2 MΩ cm@25 °C) was used for material preparation and experiments.

2.1.1. Biochar synthesis and activation

HZS_550 and UGW_550 were obtained HZS and UGW biomass under N_2 at 550 °C, with a heating rate of 10 °C min^{-1} and a residence time of 60 min.

Chemical activation: HZS_550 and UGW_550 were dispersed in 1.2 M KOH at room temperature for 60 min to produce HZS_550_KOH and UGW_550_KOH. The samples were then subjected to a second pyrolysis at 700 °C for 60 min under N_2.

Physical activation and impregnation: CO_2-activated biochars were prepared following either a *one-step* or *multi-step* activation route. The term *one-step* refers to a continuous pyrolysis/CO_2 activation process carried out within the same thermal treatment, whereas *multi-step* activation routes involve intermediate material processing, chemical impregnation, washing, and/or additional thermal treatments (see Supplementary Material).

UGW_CO_2_30 and UGW_CO_2_60 were synthesized through a one-step, continuous pyrolysis/activation route: UGW biomass was heated under N_2 (10 °C min^{-1}) to 110 °C for 30 min, then to 550 °C for 30 min, and finally activated under CO_2 at 800 °C for either 30 min (UGW_CO_2_30) or 1 h (UGW_CO_2_60). **UGW(N)_CO_2_60** was obtained via a two-step synthesis process combining pyrolysis, impregnation, and activation. After initial pyrolysis (110 °C → 550 °C), the cooled biochar was impregnated with 20 wt% imidazole or melamine ethanol solution, then re-heated under CO_2 (800 °C, 1 h, 20 °C min^{-1}). **UGW(N)_CO_2_60_P** followed a three-step route. UGW(N)_CO_2_60 (1 g) was washed with 50 mL HNO_3 and subjected to a second pyrolysis in N_2 at 900 °C (20 °C min^{-1}, 2 h).

2.1.2. Electrode preparation

Electrodes were classified as control or biochar-based.

Control electrodes: *(i)* bare carbon cloth (E0); *(ii)* carbon cloth coated with ~3 mg cm^{-2} Vulcan XC-72R + 20 wt% PTFE (E0a); *(iii)* carbon cloth coated only with 20 wt% PTFE (E0b). Coatings were applied by air-spraying, followed by heat treatment and hot pressing at a pressure of 2.5 MPa. Biochar-based electrodes were prepared using either brush painting (BP) or spray coating (SC) techniques, adapting and further developing electrode preparation methods previously optimized in our laboratories (Nisa et al., (2023) 1319.; Nisa et al., 2024).

For BP, an ink consisting of 20 mg UGW_CO_2_60, 10 μL PTFE (40 wt %), and 20 μL H_2O was brushed over a 4 cm^2 substrate, air-dried, and then heat-treated at 370 °C for 20 min, yielding the BP_UGW_MPL sample. Here, MPL denotes the microporous layer, which, in the electrode architecture, typically consists of high-surface-area carbon particles (biochar in this work) and PTFE to impart controlled hydrophobicity.

For SC, biochar and PTFE (20 wt% with respect to the solid content) were dispersed in an isopropanol/water mixture (2:1 v/v) to obtain a homogeneous ink with a biochar loading of 1 mg mL^{-1}. The suspension was sonicated for 40 min prior to deposition. The ink was spray-coated onto a preheated carbon cloth substrate at 80 °C using a 0.3 mm airbrush (Iwata HP-SBS Eclipse) supplied by a compressor (Stanley 1.0 HP 6 L 8 bar) at an operating pressure of 0.3–0.5 bar, with a nozzle-to-substrate distance of 10 cm.

After deposition, the coated samples were hot-pressed (2.5 MPa, 90 °C, 15 min) and subsequently heat-treated at 350 °C for 30 min, yielding the SC_UGW_MPL sample. Complete electrodes consisting of an MPL and a catalyst layer (CL) were prepared using the same procedure. In this electrode architecture, the CL serves as the electrochemically active layer, with the biochar providing catalytic sites for interfacial electron transfer. For the CL, the inks contained Nafion as the binder (22 wt% relative to the solid content), which provides ionic conductivity, whereas the MPL used PTFE to impart hydrophobicity. The electrodes were finally hot-pressed (2.5 MPa, 80 °C, 10 min) to obtain E1_UGW, E2_UGW(N), and E3_UGW(N)_P.

2.1.3. Physicochemical characterization of biochar and electrodes

Elemental analysis for CHNS(O) was conducted using the Vario MACRO-cube analyzer (Elemental Macro). Calibration of the instrument was achieved using a sulfanilamide standard, as specified in ISO 16948:2015. Fourier Transform Infrared Spectroscopy (FTIR) measurements were performed using a PerkinElmer FTIR 100 spectrometer in transmittance mode. Sample pellets, prepared by compressing 150 mg of potassium bromide (KBr) using a Specac manual hydraulic press under 7 tons of pressure for 5 min, had a diameter of 13 mm. Powder X-ray diffraction (XRD) patterns were acquired using a Philips PW1730 diffractometer equipped with Cu Kα radiation (λ = 1.5406 Å). Surface morphology was investigated through field-emission scanning electron microscopy (FE-SEM) using a Leo Supra 35 microscope (Carl Zeiss, Oberkochen, Germany). Raman spectroscopy was conducted using a DXR Raman Microscope (Thermo Scientific) with a 532 nm laser excitation wavelength, a 10 × objective, and a laser power of 0.1 mW. Raman spectra were processed and deconvoluted using OriginPro software (OriginLab Corporation). Prior to peak fitting, a second-order polynomial baseline subtraction was applied to account for background and fluorescence contributions. No additional smoothing or filtering was applied in order to preserve the original spectral features. Peak deconvolution was performed using Gaussian functions, primarily to qualitatively resolve overlapping Raman bands and support peak assignment. The quality of the fits was assessed by inspection of the residuals and the coefficient of determination (R^2), which typically ranged from 0.98 to 0.99.

Nitrogen adsorption–desorption isotherms were obtained using a Micromeritics® TriStar II Plus analyzer. The specific surface area was determined by the Brunauer–Emmett–Teller (BET) method. Prior to analysis, the samples were degassed under vacuum at 250 °C for 4 h to remove adsorbed impurities and subsequently loaded into the sample holders for measurement. X-ray photoemission spectroscopy (XPS) measurements were performed using an Omicron DAR 400 Mg Kα non-monochromatized X-ray source coupled to a VG-CLAM2 electron spectrometer, operated at a pass energy of 20 eV. Deconvolution of the C 1s and N 1s core levels was performed using the KolXPD software (https://kolxpd.com). Peak fitting employed Voigtian line shapes, combining weighted Gaussian and Lorentzian functions, along with Shirley background subtraction.

Electrochemical measurements were conducted in a standard three-electrode cell, with a rotating disk electrode (RDE) as the working electrode, a graphite rod as the counter, and a saturated Ag/AgCl (3.3 M KCl) reference electrode. Experiments were controlled by a VMP3 potentiostat (EC-Lab v10.18). Potentials *vs.* Ag/AgCl were converted to the reversible hydrogen electrode (RHE) scale. Electrolytes were 0.1 M phosphate buffer solution (PBS) at pH 7.4 or 0.1 M KOH. The glassy carbon disk was polished with alumina (0.3 and 0.05 μm), rinsed, and ultrasonicated before catalyst ink deposition. Catalyst inks were prepared in isopropanol/Nafion to achieve a 0.3 mg cm^{-2} loading and were ultrasonicated for 2 h at ~15 °C. Prior to ORR tests, PBS was purged with N_2 for 20 min, and the working electrode was activated by cyclic voltammetry (CV) at 0.3–1.2 V *vs.* RHE at 500 mV s^{-1} for 200 cycles. CV and linear-sweep voltammetry (LSV) were used to record capacitive and ORR currents after purging with N_2 or O_2. LSV was performed at 5 mV s^{-1} and an electrode rotation rate of 1600 rpm. Capacitive contributions were corrected by subtracting N_2-saturated currents, and potentials were iR-corrected, using the uncompensated resistance obtained from electrochemical impedance spectroscopy by fitting the high-frequency region with a Randles-type equivalent circuit. The double-layer capacitance (C_{dl}) was evaluated by acquiring CVs in a −0.5–0.0 V *vs.* Ag/AgCl potential window at scan rates ranging from 5 to 100 mV s^{-1} in a N_2-saturated 0.1 M PBS. C_{dl} was estimated by calculating the slope (s) of the linear fit of the anodic current density at −0.3 V *vs.* Ag/AgCl as a

function of the scan rate. The specific electrochemically active surface area (ECSA) was then calculated using Eq. (1):

$$ECSA = \frac{s}{mC_s} \quad (1)$$

where s is the slope (mF), m is the mass of biochar on the electrode (g), and C_s is the specific capacitance taken as 0.3 Fm^{-2} (Pepè Sciarria et al., 2020). All measurements were performed in three independent replicates, and the values reported in the tables are expressed as the average ± standard deviation.

2.1.4. Preliminary test in microbial electrosynthesis cell

The produced electrodes (E0b, E1, E2, and E3) were tested as cathodes in MES for 21 days. MES consisted of two chambers separated by Nafion 117 proton-exchange membrane (DuPontTM, US). The anode was a 1 x 4 cm anodized titanium mesh. MES cathodes were inoculated with the organic fraction of municipal solid waste (OFMSW) pre-acclimated inoculum and modified medium as described in previous reports (Patil et al., 2015) with 1.25 g L^{-1} of NH_4Cl. The cathodes were polarized at −1.0 V *vs.* Ag/AgCl using a potentiostat in chronoamperometry mode (NEV4, Nanoelectra S.L., Spain). Cyclic voltammetry was recorded at a potential range of −1.0 V to 0.5 V *vs.* Ag/AgCl with a scan rate of 1 mV s^{-1}. The short experimental duration was intentionally selected to rapidly provide preliminary indications of the electrodes' stability in a bioelectrochemical reactor and their interaction with the microbial consortium. This preliminary assessment focused on early-stage microorganism-electrode interactions and potential cathode instability phenomena, including biochar detachment, early biofouling, and pH gradient issues. Product quantification and efficiency indicators (e.g., Coulombic efficiency) were deliberately not evaluated at this stage, as they require longer-term, steady-state operation and fall outside the scope of this preliminary chapter and of this materials-oriented study. These aspects will be specifically addressed in a subsequent experiment focusing on microbial electrosynthesis using the selected cathodes.

A preliminary microbial community analysis was conducted on the starting inoculum (OFMSW) and lyophilized biomass to evaluate differences between the original source, biochar-modified, and control electrodes and to confirm that the microbial assemblages developing in the system would be consistent with the underlying physiology expected in such microbial electrosynthesis cells. DNA was extracted from OFMSW and lyophilized biomass (DNeasy PowerSoil Pro Kit, Qiagen, Hilden, Germany), and the V3–V4 region of the 16S rRNA gene was sequenced on an Illumina NovaSeq 6000 platform (250 bp paired-end) by Novogene Co. Ltd. (Cambridge, UK). Sequences were processed with QIIME2 (Bolyen et al., 2019), and ASVs (amplicon sequence variants) were taxonomically assigned using the Greengenes2 database (version 2024.09 (McDonald et al., 2024). ASV table, taxonomy table, and sample metadata were imported into RStudio (version 2024.04.2 + 764) and combined in a single object with the microeco package (Liu et al., 2021). ASVs with total counts ≤ 5 were filtered out, along with those that did not belong to the Bacteria or Archaea kingdoms, and ASVs annotated as Mitochondria or Chloroplast. The count data were normalized using Total Sum Scaling (TSS) to convert raw counts into relative abundances. All statistical analyses and visualizations were performed in RStudio using different packages (microeco, vegan, emmeans, and ggplot2). Taxonomic bar plots were generated, displaying the 20 most abundant taxa for each sample group.

Alpha diversity was assessed to characterize microbial diversity across five experimental groups (OFMSW, MES E0b, MES E1, MES E2, and MES E3), using the Shannon index as the primary measure of richness and evenness. Sequencing depth ranged from 2,453 to 26,318 reads per sample. To avoid data loss due to uneven library sizes, rarefaction was avoided, and sequencing depth was explicitly included as a covariate in statistical models. A linear model was fitted with Shannon diversity as the response variable, experimental group as a fixed effect, and log-transformed sequencing depth as a covariate. Group effects were evaluated via ANOVA, and pairwise comparisons were performed using estimated marginal means with Benjamini-Hochberg correction to control for multiple testing.

Beta diversity was assessed to evaluate differences in microbial community composition among experimental groups using the normalized dataset. Bray-Curtis dissimilarity was calculated and visualized using Principal Coordinates Analysis (PCoA) to examine clustering patterns. The effect of the experimental group on community composition was tested using permutational multivariate analysis of variance (PERMANOVA, adonis2), with R^2 and p-values reported to quantify the proportion of variation explained.

All statistical analyses and visualizations were performed in Rsudio, using the microeco, vegan, emmeans, and ggplot2 packages.

3. Results and Discussion

3.1. Optimization of Biomass-Derived biochars via pyrolysis and activation

Elemental analysis (CHNS) of the feedstocks (UGW and HZS) and their corresponding biochars obtained by slow pyrolysis at 550 °C (HZS_550 and UGW_550, respectively) is reported in Table 1, together with BET surface area values. The two feedstocks exhibit comparable compositions, except that UGW contains more than ten times the nitrogen content of HZS, as well as trace amounts of sulfur. Moreover, the elemental composition of the biochar samples is consistent with previous findings reported in the literature (Chaudhary et al., 2023; Zhao et al., 2024). After pyrolysis, HZS_550 exhibited a larger specific surface area than UGW_550.

Chemical activation with KOH was subsequently applied to enhance porosity and introduce hydrophilic functional groups, a key feature for preparing catalytic inks in electrochemical applications. This treatment led to an 18 % increase in BET surface area for the UGW-derived biochar (from 145 to 172 m^2 g^{-1}, as reported in Table 1), whereas the HZS sample did not exhibit a significant change. SEM images confirmed that KOH activation effectively opened the pore structure, particularly in the UGW sample (see Supplementary Material).

Interestingly, the higher BET surface area of the HZS-based sample was not reflected in a larger electrochemical surface area. The

Table 1
Elemental analysis and BET surface area (SA) analysis for biochar-based samples.

Sample	C (wt.%)	H (wt. %)	N (wt. %)	S (wt. %)	O + ashes (wt.%)	BET SA (m^2g^{-1})
HZS (feedstock)	46.64 ± 0.11	6.24 ± 0.66	0.08 ± 0.01	–	47.04 ± 0.09	–
HZS_550	78 ± 1	1.4 ± 0.1	0.20 ± 0.01	–	20.4 ± 0.2	333 ± 10
UGW (feedstock)	45.27 ± 0.65	5.96 ± 0.90	0.84 ± 0.08	0.03 ± 0.01	47.90 ± 1.55	–
UGW_550	69.70 ± 0.59	0.85 ± 0.33	1.30 ± 0.09	0.11 ± 0.02	28.04 ± 0.89	145 ± 4.3
UGW_550_KOH	69.28 ± 2.66	0.25 ± 0.03	0.84 ± 0.07	0.55 ± 0.07	29.08 ± 2.84	172 ± 5.2
UGW_CO_2_30	67.87 ± 0.6	0.26 ± 0.03	1.85 ± 0.06	0.44 ± 0.06	29.58 ± 0.86	486 ± 15
UGW_CO_2_60	71.09 ± 2.36	0.28 ± 0.10	1.79 ± 0.07	0.58 ± 0.23	26.26 ± 2.13	546 ± 14
UGW(N) _CO_2_60	72.58 ± 1.37	0.28 ± 0.14	2.80 ± 0.08	0.46 ± 0.11	23.88 ± 3.13	450 ± 14
UGW(NM) _CO_2_60	61.62 ± 2.91	0.52 ± 0.14	2.50 ± 0.05	0.19 ± 0.11	35.17 ± 3.13	336 ± 10
UGW(N) _CO_2_60_P	75.2 ± 0.58	0.64 ± 0.04	2.90 ± 0.06	0.09 ± 0.01	21.17 ± 0.75	613 ± 18

electrochemically active surface area (ECSA), estimated through the double-layer capacitance (C_{dl}) obtained from cyclic voltammetry at varying scan rates, was 1.93 mF cm^{-2} for UGW_550_KOH and 1.00 mF cm^{-2} for HZS_550_KOH. This indicates that the UGW-derived material provides superior electrochemical accessibility despite its lower BET surface area. A notable opposite trend between BET and ECSA has been previously reported (Pepè Sciarria et al., 2020) and attributed to differences in surface chemistry and the balance of hydrophobicity and hydrophilicity in biochar. In addition to pore size and connectivity, the electrochemical accessibility of biochar surfaces is strongly influenced by surface wettability and the spatial distribution of surface functional groups. Oxygen-containing functional groups can enhance electrolyte wetting and ion transport, thereby increasing the fraction of BET surface area that is electrochemically accessible. Conversely, hydrophobic domains or non-uniform functionalization may limit electrolyte transport into microporous regions, contributing to lower ECSA values despite high BET surface areas (Trasatti and Petrii, 1992). Furthermore, BET measurements are typically performed on powdered materials, whereas ECSA is determined on a deposited film of biochar and binder (e.g., Nafion) on a conductive electrode surface (such as glassy carbon), which more accurately reflects the number of electrochemically active sites under operating conditions (Nagai and Ioroi, 2025; An et al., 2024). The ECSA of an electrocatalyst is therefore more meaningful than its geometric specific surface area obtained by the BET method, as it directly correlates with the density of active sites available for electrochemical reactions (Raveendran et al., 2023). These considerations are

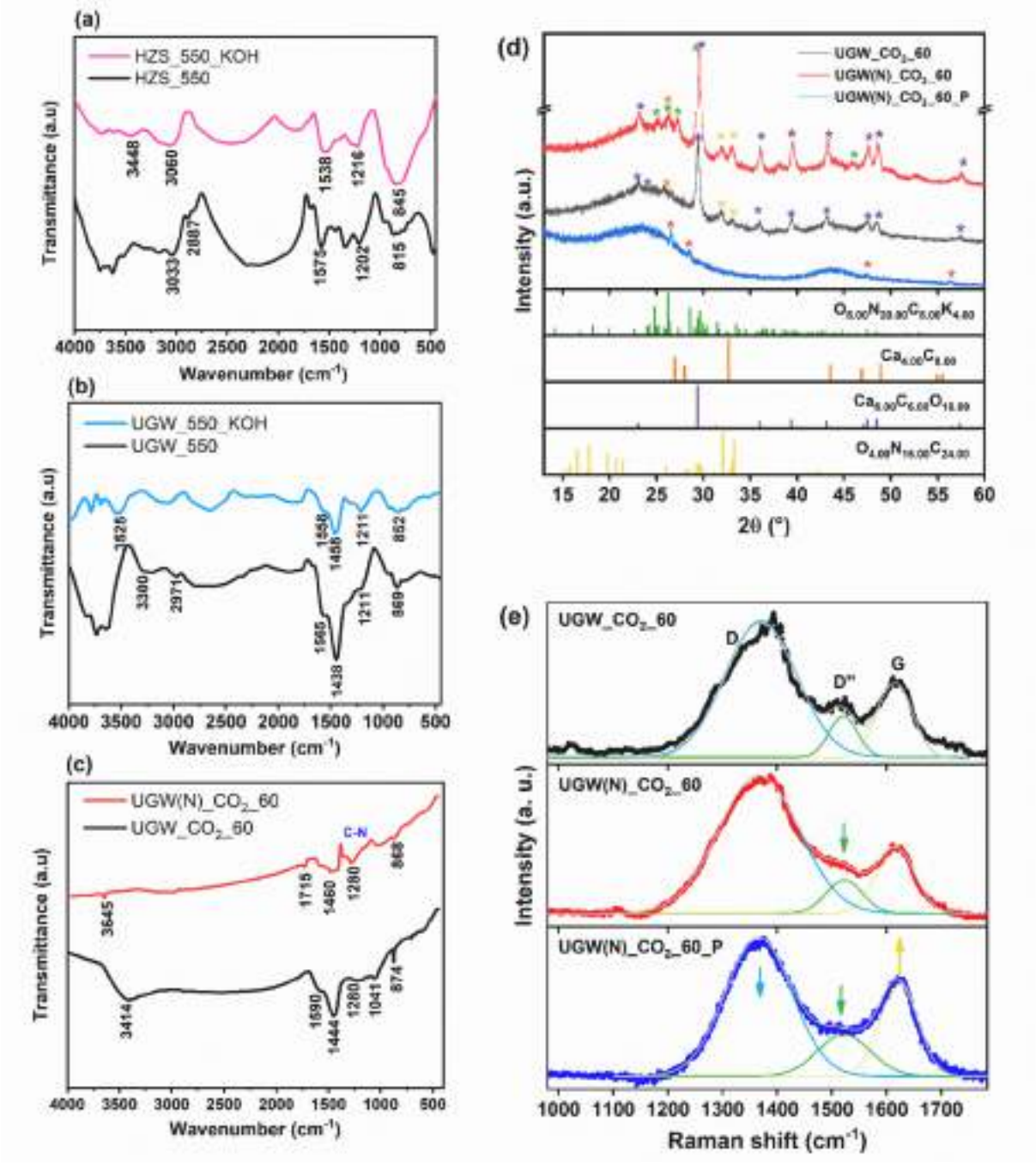

Fig. 1. FTIR spectra of HZS_550_KOH and HZS_550 (a), UGW_550_KOH and UGW_550 (b), and UGW(N)_CO_2_60 and UGW_CO_2_60 (c), XRD patterns (d) and Raman spectra (e) of UGW_CO_2_60, UGW(N)_CO_2_60, and UGW(N)_CO_2_60_P.

particularly relevant for biochar-based electrodes, where structural heterogeneity, non-uniform functionalization, and film deposition effects combine to determine the effective electrochemical surface area and catalytic performance. Additionally, the interplay of functional groups and wetting behavior can strongly modulate electrochemical accessibility, emphasizing that BET alone may overestimate the number of truly active sites in porous biochar electrodes (Mosch et al., 2016).

FTIR analysis was performed to characterize the surface chemistry of the biochars, providing additional insight into the differences in wettability and functional group distribution that contribute to the observed discrepancies between BET surface area and ECSA (Fig. 1a and 1b). The FTIR spectra of the HZS_550 and UGW_550 samples, along with their KOH-activated counterparts, exhibit characteristic bands in the region of 3640–3300 cm^{-1}, which can be attributed to the stretching vibrations of hydrogen-bonded hydroxyl groups. A band observed around 3060 cm^{-1} for the HZS-based sample (Fig. 1a) corresponds to C—H stretching of substituted aromatic carbons, while the bands between 2970 and 2870 cm^{-1}, evident for HZS_KOH and UGW_KOD, are assigned to the symmetric C—H stretching of aliphatic $–CH_x$ groups (Sajjadi et al., 2019). Bands in the region of 1580–1440 cm^{-1} are associated with C═C stretching of aromatic components, the shift to lower wavenumbers for the band of UGW-based biochar as compared to HZS-based biochar suggesting that the C═C stretching arises from lignin, as expected given the nature of the UGW precursor (Janu et al., 2021). The band in the region 1200–1220 cm^{-1}, related to C═O stretching, is enhanced in the KOH activated samples, whereas the band between 869 and 815 cm^{-1}, attributed to the C—H out-of-plane bending of aromatic CH groups (Keiluweit et al., 2010), is reduced upon KOH activation. This trend suggests that activation promotes the removal of residual volatiles and increases biochar surface area and hydrophilicity. The spectral modifications associated with activation are more pronounced in UGW-based biochars than in HZS-based samples, indicating greater removal of residual volatiles and increased surface area and hydrophilicity. These results are consistent with the capacitive current analysis, suggesting that the enhanced development of oxygen-containing functional groups and decreased aromaticity in UGW contribute to a higher electrochemically accessible surface area and increased hydrophilicity, both of which can promote electrocatalytic activity. Therefore, UGW demonstrates greater potential than HZS as a feedstock for optimizing pyrolysis and activation protocols for electrode production.

In addition to KOH activation, physical activation with CO_2 was explored as an alternative to reduce chemical use and assess the feasibility of a one-step activation process. CO_2 activation was performed directly from the UGW feedstock via a one-step thermal treatment, in contrast to KOH activation, which requires a more complex multi-step sequence involving two pyrolysis stages intercalated with a chemical treatment.KOH activation resulted in a 35 % loss of nitrogen functionalities compared to the initially pyrolyzed material, as indicated by the elemental analysis results presented in Table 1. By contrast, CO_2 activation preserved nitrogen and even enhanced its content. Specifically, the nitrogen content increased up to ~1.8 wt% after CO_2 activation, compared to both the pristine UGW feedstock (0.84 wt%) and the non-activated sample UGW_500 (1.30 wt%), indicating that this one-step process effectively valorizes the inherent nitrogen contained in UGW. Additionally, CO_2 activation proved more effective than KOH in enhancing the textural properties. The increase in surface area was strongly time-dependent, as evidenced by the values obtained after 30 and 60 min of CO_2 flow (Table 1). The optimized sample, UGW_CO_2_60, exhibited the highest surface area (546 m^2g^{-1}) and a double-layer capacitance of 9.2 mF cm^{-2}, as determined by cyclic voltammetry at varying scan rates. These results identify UGW_CO_2_60 as the most promising material, owing to its high nitrogen content, developed porosity, and superior capacitive behavior. Consequently, UGW_CO_2_60 was selected not only for subsequent detailed electrochemical investigations but also as a platform for further processing, including nitrogen enrichment via external precursors and tailoring the degree of graphitization through additional pyrolysis at higher temperatures.

3.2. Nitrogen functionalization and Post-Treatment of biochars

To increase nitrogen content and modify the surface chemistry of UGW-derived biochar, a multi-step functionalization was applied. The process included pyrolysis at 550 °C, impregnation with nitrogen-rich organic precursors, and CO_2-mediated activation. Two precursors were used: imidazole (with two N atoms) and melamine (with six N atoms), yielding UGW(N)_CO_2 and UGW(N_M)_CO_2, respectively. Impregnation enhanced nitrogen incorporation compared to non-functionalized UGW_CO_2_60 (Table 1), with imidazole proving more effective than melamine, consistent with reports of superior nitrogen doping and electrocatalytic performance from imidazole-type precursors (W. da S. Freitas et al., 2021; da Silva Freitas et al., 2022). In both cases, functionalization decreased surface area compared to UGW_CO_2_60 (Table 1). To understand the impact of nitrogen impregnation, FTIR spectroscopy was performed to provide insights into the functional groups present, particularly those resulting from CO_2 activation and nitrogen modification. Fig. 1(c) shows the FTIR spectra of UGW_CO_2_60 and UGW(N)_CO_2_60.

A broad band associated with –OH stretching was detected around 3400 cm^{-1} in UGW_CO_2_60, which becomes significantly narrower and shifts to higher wavenumbers (3640 cm^{-1}) in UGW(N)_CO_2_60, reflecting changes in hydrogen bonding due to the introduction of nitrogen groups that alter the –OH environment. In the 1700–1600 cm^{-1} region, UGW(N)_CO_2_60 exhibits a band corresponding to C═O stretching vibrations, suggesting the presence of carbonyl groups in conjugated ketones and quinones (Janu et al., 2021). UGW(N)_CO_2_60 also displays new bands between approximately 1266 and 1342 cm^{-1}, corresponding to the stretching vibrations of C—N amines (Liu et al., 2015; Yan et al., 2016), confirming successful nitrogen functionalization and incorporation into the biochar matrix. In the lower-wavenumber region, UGW_CO_2_60 shows a band at 1041 cm^{-1}, attributed to C—O—C symmetric stretching in aliphatic groups and acid derivatives (Calderón et al., 2006). This disappearance is likely due to the introduction of nitrogen functionalities, which modify the local chemical environment of the original oxygen-containing groups.

UGW(N)_CO_2 was subjected to a further post-treatment consisting of nitric acid washing followed by high-temperature pyrolysis, yielding the material UGW(N)_CO_2_P. This procedure resulted in a further increase in surface area (Table 1) while maintaining the incorporated nitrogen at 2.9 wt%, thereby combining improved textural properties with enhanced nitrogen functionalities.

The X-ray diffraction (XRD) and Raman spectroscopy analyses of UGW_CO_2_60, UGW(N)_CO_2_60, and UGW(N)_CO_2_60_P provide important insights into their crystalline phase composition and carbon structural order. The XRD patterns (Fig. 1(d)) highlight differences in crystallinity and the presence of nitrogen-containing phases. All biochar samples show broad diffraction peaks at $2\theta \approx 25^\circ$ and $2\theta \approx 45^\circ$, characteristic of the amorphous carbon structure typically observed in biochar. UGW_CO_2_60 and UGW(N)_CO_2_60 display additional crystalline phases based on calcium carbonates, namely calcite ($Ca_6C_6O_{18}$) and calcium carbide (Ca_4C_8). Furthermore, all samples exhibit crystalline phases incorporating nitrogen, such as potassium 1,3-dinitrate-2,2-bis (nitratomethyl)propane ($O_8N_{20}C_8K_4$). In addition, UGW_CO_2_60 and UGW(N)_CO_2 contain tetrahexacyanoethylene oxide ($O_4N_{16}C_{24}$). The UGW(N)_CO_2_P sample shows sharper peaks at $2\theta = 25^\circ$ and $2\theta = 45^\circ$, suggesting higher crystallinity and a more graphitic structure (Fu et al., 2017), while only trace amounts of calcium hydrocarbons are detected.

The Raman spectra (Fig. 1(e)) provide complementary insight into the degree of graphitization, structural disorder, and the effects of nitrogen doping and pyrolysis. All samples display two main features: the D band (~1370 cm^{-1}), associated with disordered or amorphous carbon, and the G band (~1610 cm^{-1}), attributed to sp^2-hybridized carbon

in graphitic domains. A shoulder around 1525 cm^{-1}, corresponding to the D'' band, is also observed in all spectra, reflecting disordered sp^2-bonded structures and interstitial defects (Mecheri et al., 2018).

Deconvolution of the spectra into three components (D, G, and D") enables the evaluation of structural disorder through the I_D/I_G intensity ratio, which is a common indicator of graphitization. Higher I_D/I_G values denote increased defect density and lower structural order. UGW_CO_2_60 exhibits an I_D/I_G ratio of 1.87, characteristic of a highly disordered, amorphous carbon framework, consistent with biochars obtained under similar conditions (Liu et al., 2018; Ferrari, 2007). UGW(N)_CO_2_60 exhibits a slightly higher ratio (2.07), suggesting that nitrogen incorporation introduces additional defects, likely associated with C—N and N—H bonding, which perturbs the sp^2 carbon network. In contrast, UGW(N)_CO_2_60_P, subjected to pyrolysis at 900 °C, exhibits a reduced I_D/I_G ratio of 1.42, indicating enhanced graphitization and the formation of more ordered graphitic domains while retaining a partial nitrogen content.

Raman and XRD results are corroborated by SEM analysis of UGW_CO_2_60, UGW(N)_CO_2_60, and UGW(N)_CO_2_60_P at 10–50 kX magnification (Fig. 2). Clear morphological differences arise from nitrogen incorporation and subsequent pyrolysis. UGW_CO_2_60 (Fig. 2a–c) shows a rough, highly porous surface with irregular cavities typical of untreated biochar. In contrast, UGW(N)_CO_2_60 (Fig. 2d–f), functionalized with imidazole, exhibits a heterogeneous texture characterized by bubble-like domains and nanoparticle aggregates, likely formed through partial interactions between imidazole residues and inorganic phases. Correspondingly, diffraction peaks between 30°–35°, assigned to potassium 1,3-dinitrate-2,2-bis(nitratomethyl)propane ($O_8N_{20}C_8K_4$), appear more intense than in UGW_CO_2_60. After pyrolysis at 900 °C, UGW(N)_CO_2_60_P (Fig. 2g–i) exhibits a more compact and layered morphology with smoother surfaces and smaller, ordered pores. This evolution confirms the role of high-temperature treatment in removing volatiles, enhancing graphitization, and reducing structural disorder, consistent with XRD and Raman analyses.

3.3. Electrochemical evaluation of biochar, electrode preparation, and MES applications

To evaluate the intrinsic electrocatalytic activity of the biochars prior to electrode fabrication, we selected the oxygen reduction reaction (ORR), a well-studied process relevant to bioelectrochemical systems such as microbial fuel cells (Aysla Costa De Oliveira et al., 2020; Li et al., 2021; Santoro et al., 2020). The electrochemically active surface area (ECSA) was determined by cyclic voltammetry at different scan rates under neutral conditions (0.1 M phosphate buffer solution, pH 7.4, N_2-saturated). As shown in Fig. 3a, the capacitive current of UGW_CO_2_60 (taken as representative of the series; CVs of the other samples are reported in the Supplementary Material) increases linearly with the scan rate. From the slope of the current density *vs*. scan rate plot, a Cdl of 1.80 mF was determined, corresponding to an ECSA of 103 $m^2\ g^{-1}$. UGW(N)_CO_2_60 and UGW(N)_CO_2_60_P exhibited higher C_{dl} values of 3.31 and 4.65 mF, corresponding to ECSAs of 190 and 266 $m^2\ g^{-1}$, respectively. The enhanced ECSA of UGW(N)_CO_2_60_P is attributed to its higher degree of graphitization combined with effective nitrogen doping. Notably, despite the lower BET surface area of UGW(N)_CO_2_60 compared to UGW_CO_2_60 (Table 1), its ECSA is almost twice as high (190 *vs.* 103 $m^2\ g^{-1}$), underlining the crucial role of *N*-doping in enhancing the electrochemical accessibility of active sites (Lian et al., 2016; Wang et al., 2017).

The catalytic activity toward ORR was further investigated by linear sweep voltammetry (LSV) with a rotating disk electrode under O_2-saturated conditions at neutral pH (Fig. 3b). A clear positive shift in both the ORR onset potential (E_{onset}) and half-wave potential ($E_{1/2}$) is observed across the UGW-derived biochars, following the order UGW_CO_2_60 < UGW(N)_CO_2_60 < UGW(N)_CO_2_60_P. Specifically, UGW(N)_CO_2_P exhibits the most positive onset potential (E_{onset} = 0.84

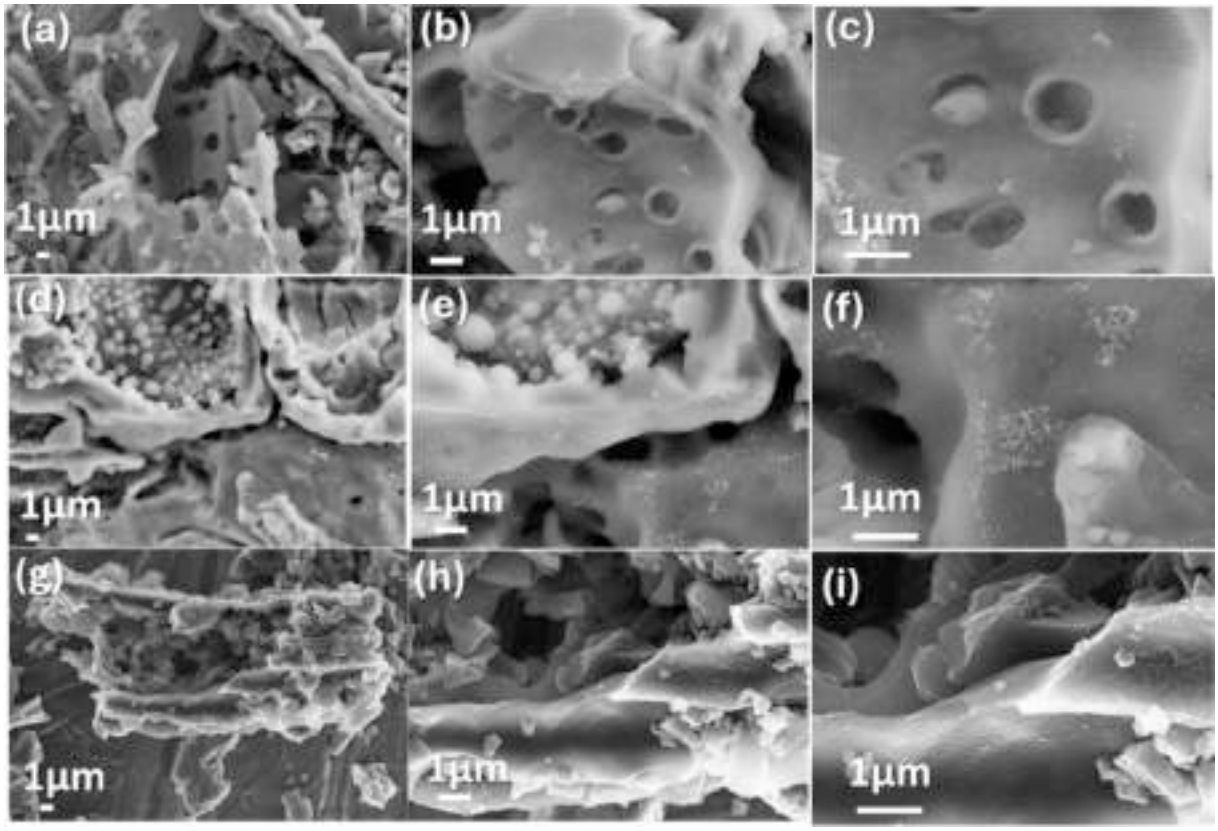

Fig. 2. SEM micrographs of UGW_CO_2_60 (a) to (c); UGW(N)_CO_2_60 (d) to (f), and UGW(N)_CO_2_60_P (g) to (i), at 10, 25, and 50 kX magnifications, respectively.

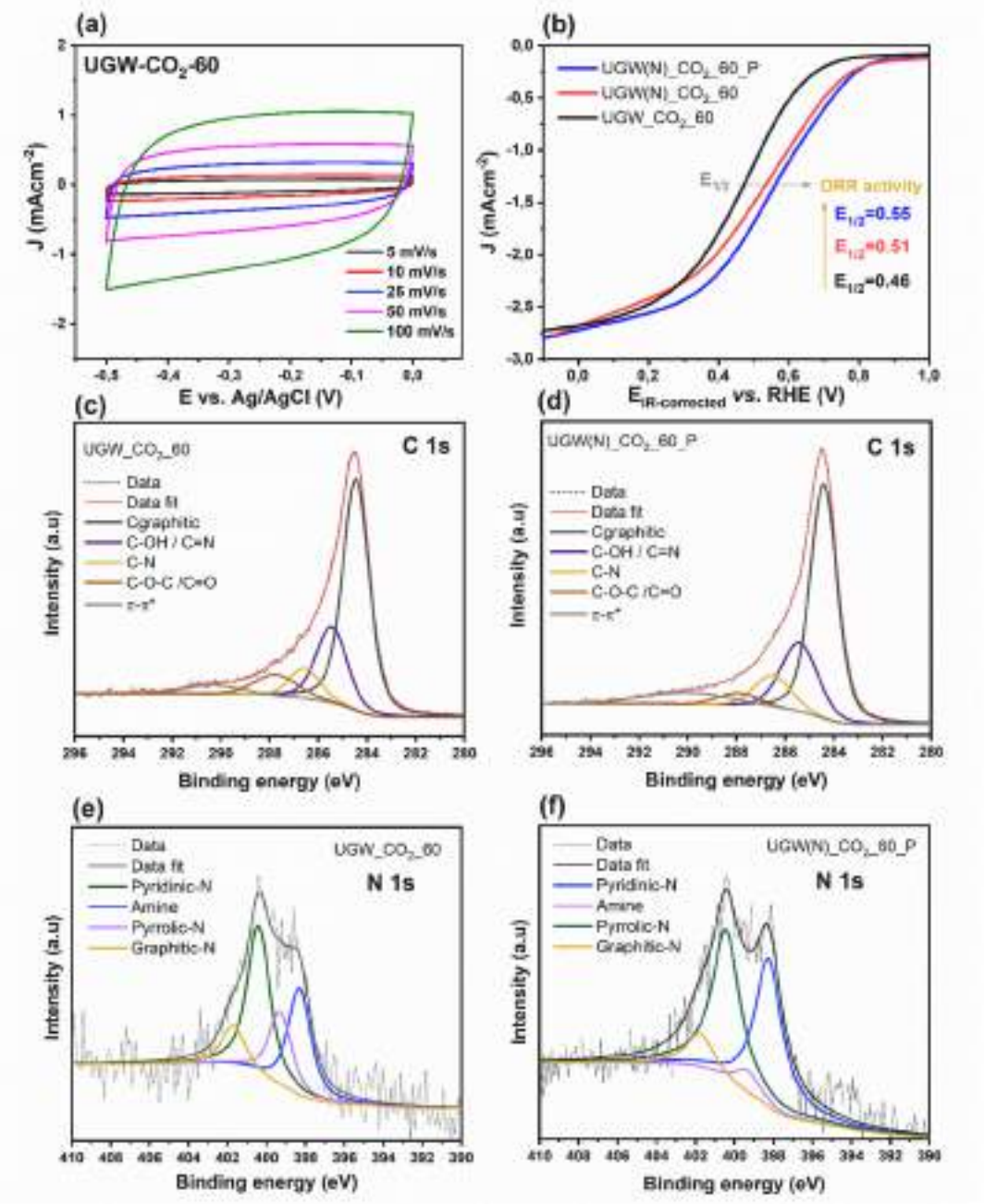

Fig. 3. CV curves at different scan rates in N_2-saturated 0.1 M PBS electrolyte for UGW_CO_2_60, (b) LSV O_2-saturated electrolyte at 1600 rpm electrode rotation, deconvolution of (c-d) C 1s and N 1s (e-f) XPS spectra of UGW_CO_2_60 and UGW(N)_CO_2_60_P.

V *vs*. RHE) and half-wave potential ($E_{1/2}$ = 0.55 V *vs*. RHE), consistent with its enhanced graphitic structure and increased active site density. These values fall within the range reported for other metal-free biochar-based catalysts (Pepè Sciarria et al., 2020; Zhang et al., 2019; Zhang et al., 2020). For comparison, benchmark ORR catalysts such as commercial Pt/C and Fe—N—C typically exhibit more positive onset (E_{onset} = 0.95–0.98 V) and half-wave potentials ($E_{1/2}$ = 0.8–0.92 V) in acidic and alkaline media (Xie et al., 2025; Hu et al., 2021; Chen et al., 2025; Q. Jia et al., 2015; Ramaswamy and Mukerjee, 2011). The lower activity observed here is therefore consistent with the metal-free nature of the present materials and the different ORR mechanisms involved (Hu et al., 2021). Importantly, the activity trend within the UGW-derived series suggests that surface chemical composition and functional group distribution play a key role. To clarify this aspect, XPS analysis was carried out.

The surface composition of UGW_CO_2_60, UGW(N)_CO_2_60, and UGW(N)_CO_2_60_P was investigated by XPS. Survey spectra (see Supplementary Material) indicate that the surface is mainly composed of carbon and oxygen, with lower contributions from calcium and nitrogen. Notably, UGW(N)_CO_2_60_P shows a significant reduction of the Ca 2p signal at 351.7 eV, indicating the effective removal of calcium-based phases after acidic leaching, in agreement with XRD results.

Fig. 3c–3f show the C 1s and N 1s spectra of UGW_CO_2_60 and UGW(N)_CO_2_60_P. The corresponding spectra for UGW(N)_CO_2_60, along with the relative percentages of all identified carbon- and nitrogen-containing functional groups, are reported in the Supplementary Material. The C 1s spectra of all samples confirm the presence of a carbon matrix functionalized with oxygen- and nitrogen-containing surface groups. A comparison among the three samples highlights the effect of the post-treatment (nitric acid washing followed by pyrolysis at 900 °C,

UGW(N)_CO_2_60_P). An increase in the C–OH/C═N component at approximately 285.4 eV is observed, with the C═N contribution likely associated with imine- or graphitic-N species. Conversely, the C—N component at around 286.5 eV, typically attributed to amine- and pyrrolic-N, decreases after post-treatment, although the overall variations are relatively small. Deconvolution of the N 1s spectra indicates that nitrogen functionalization of the biochar carbon matrix comprises pyridinic, amine, pyrrolic, and graphitic nitrogen species. Among these groups, pyridinic- and graphitic-N are well known to enhance the activity and durability of ORR in metal-free (N_x–C) and M—N—C catalysts (Rojas-Carbonell et al., 2018; Artyushkova et al., 2015; Kumar et al., 2023; Parsa et al., 2025). Comparison of the N 1s spectra of UGW_CO_2_60 and UGW(N)_CO_2_60 (see Supplementary Material) shows that imidazole functionalization mainly increased the graphitic-N content by 37.3 %, while pyridinic-N decreased by 17.3 %. After post-treatment, pyridinic-N increases significantly by 71 % in UGW(N)_CO_2_60_P, accompanied by decreases in graphitic-N (36 %) and in low-activity *N*-based groups such as amine-N (68 %). These results confirm the beneficial effect of acidic leaching combined with the pyrolysis at 900 °C in decreasing the presence of inactive phases while enhancing the formation of more active catalytic sites. This trend aligns with relevant studies, indicating that pyrolysis between 850 and 950 °C is an optimal temperature range for improving the formation of pyridinic-N, enhancing ORR activity, while promoting the graphitization of the carbon matrix, which is crucial for restraining carbon corrosion under the operating conditions of several electrochemical devices (Huang et al., 2021; Kumar et al., 2023; Qu et al., 2021; Zitolo et al., 2015; Pardo Pérez et al., 2018; Mehmood et al., 2022).

Biochar-based electrodes were fabricated using brush painting and spray-coating techniques, as described in the Experimental Section. A complete list and description of all prepared electrodes are provided in the Supplementary Material. Brush painting, even at higher loadings (5 mg cm^{-2} *vs.* 3 mg cm^{-2}), resulted in only partial coverage of the carbon cloth fibers. Spray-coating produced uniformly coated fibers, minimizing local heterogeneities that could lead to uneven electrochemical activity due to regions dominated by either the support carbon or the biochar. Consequently, spray-coating was selected as the preferred fabrication method.

Cyclic voltammetry in N_2-saturated 0.1 M PBS was performed on E0a, SC_UGW_MPL, and E1_UGW electrodes (Fig. 4a). The biochar-based MPL (SC_UGW_MPL) exhibited a higher current than the commercial carbon black MPL (E0a), indicating enhanced capacitive behavior and increased ECSA. Deposition of the catalyst layer (E1_UGW) further improved the current response, confirming the optimized architecture of the spray-coated MPL + CL with biochar. CVs recorded over an extended potential range (Fig. 4b) for E0b, E1_UGW, E2_UGW(N), and E3_UGW(N)_P (hereafter E1, E2, and E3) revealed a progressive shift of the HER onset from –1.6 V to –1.2 V *vs.* Ag/AgCl, demonstrating that biochar incorporation enhances intrinsic catalytic activity toward hydrogen evolution. Nitrogen functionalization and post-treatment further enhanced HER kinetics, as reflected by the current densities measured at –0.6, –1.0, and –1.5 V, which increased in the same order. The control electrode (E0b) showed negligible current compared with the biochar-modified electrodes, confirming the beneficial effect of the biochar-based modifications on electrocatalytic performance. It has been previously reported that, although metal-free carbon-based materials can exhibit intrinsic electrocatalytic activity toward the HER, such activity generally occurs at significantly higher overpotentials than in metallic electrocatalysts (Naik et al., 2025; Ahmed et al., 2025; Feidenhans'l et al., 2024). In this context, heteroatom doping, particularly nitrogen, has been shown to play a key role by modifying the electronic structure, enhancing proton adsorption, and generating catalytically active defect sites that promote hydrogen evolution. Consequently, performance improvements in metal-free carbon electrocatalysts are commonly evaluated in terms of relative kinetic trends, such as shifts in onset potential and systematic increases in current density, rather than absolute numerical benchmarking metrics (Samanta and Pradhan, 2025).

The differences in electrochemical properties among the three biochars are more pronounced on glassy carbon RDEs compared to carbon cloth electrodes, where the variations are relatively marginal. This attenuation can be primarily attributed to the higher biochar loading and thicker films on the carbon cloth, as well as the higher percentage of Nafion, ~ 9 wt% for RDE experiments *versus* 22 wt% in the electrode's catalyst layer, together with 20 wt% PTFE composing the MPL. The presence of PTFE and a higher Nafion content affect charge transport and modulate the measured electrochemical response relative to the minimal, well-dispersed films on RDEs. This attenuation is a common observation reported in the literature: many studies indicate that clear differences in the electrochemical properties of materials (*i.e.*, biochar, Pt/C, oxides) are readily observed in thin, well-dispersed films on RDEs, whereas when the same materials are integrated into thicker layers on supports such as carbon cloth or in the MEA configuration, these differences tend to diminish (Imhof et al., 2023; Ehelebe et al., 2022).

The prepared biochars, as determined by textural, structural, and electrochemical characterization, exhibited favorable properties for electrocatalytic applications in bioelectrochemical system electrodes. Accordingly, the biochar-based electrodes were subjected to preliminary tests in MES reactors for CO_2 electroreduction, as reported in Section 2.2.2. During 21-day chronoamperometric experiments, the average current values of the three biochar-based electrodes were consistently

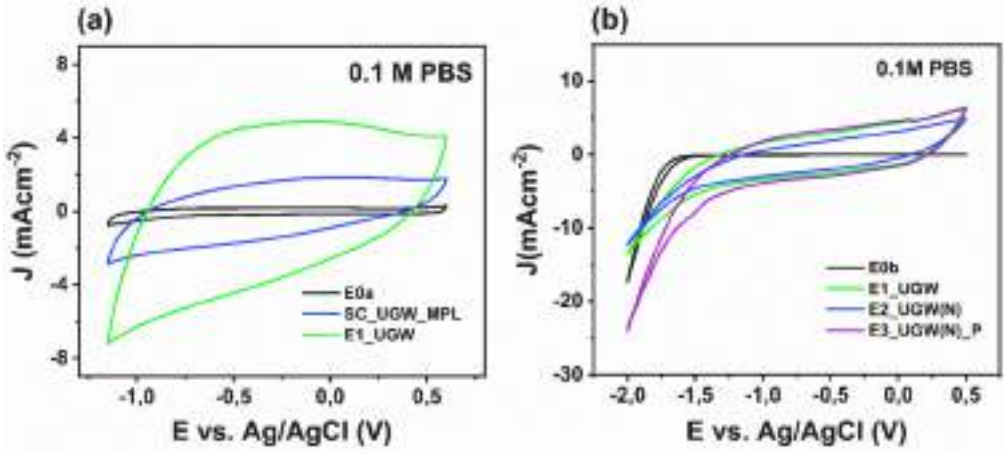

Fig. 4. CV profile in N_2-saturated 0.1 M PBS as electrolyte of (a) E0a, SC_UGW_MPL, and E1_UGW, potential window: −1.15 to 0.6 V *vs.* Ag/AgCl, scan rate 10 mVs^{-1} (a), E0b, E1_UGW, E2_UGW(N), and E3_UGW(N)_P, Potential window: −2.0 to 0.5 V *vs.* Ag/AgCl, scan rate 3 mVs^{-1} (b).

higher than those of the biochar-free control (E0b). Specifically, average currents of –5.07 ± 3.04 mA (–0.24 ± 0.14 mA cm^{-2}) for E2, –3.99 ± 1.49 mA (–0.19 ± 0.07 mA cm^{-2}) for E1, and –3.74 ± 1.40 mA (–0.18 ± 0.07 mA cm^{-2}) were recorded, compared to –2.90 ± 1.00 mA (–0.14 ± 0.05 mA cm^{-2}) for the control.

These findings were further supported by cyclic voltammetry experiments conducted at the end of the MES tests, which are shown in the supplementary material. The CVs recorded in inoculated MES systems revealed clear differences between the control cathode (E0b), which showed a narrow, steep curve, and the biochar-functionalized cathodes, which displayed broader curves and higher current densities. These results indicate an enhanced electron transfer capacity and higher reducing power at the cathode for the biochar-based electrodes, which may promote CO_2 fixation and stimulate microbial growth (Goglio et al., 2025; Soggia et al., 2024; Zheng et al., 2024).

3.4. Microbial community analysis

The starting inoculum was primarily characterized by the families Rhizobiaceae, Flavobacteriaceae, Cellulomonadaceae, Mycobacteriaceae, Micrococcaceae, Devosiaceae, and Microbacteriaceae. However, in MES systems, these families were drastically reduced or disappeared, giving rise to distinct microbial communities.

This conclusion is further supported by microbial analysis of the lyophilized biomass developed in MES (Fig. 5). In MES systems with biochar-modified electrodes, the microbial community was enriched in the phyla Bacteroidota, Bacillota, and Campylobacterota, including families such as Clostridiaceae, Eubacteriaceae, and Sulfurimonadaceae. In contrast, MES with unmodified electrodes was dominated by the phylum Pseudomonadota, particularly the Rhizobiaceae and Rhodobacteraceae families (Fig. 5).

Alpha diversity, as measured by the Shannon index (Fig. 6a), differed among the five experimental groups. OFMSW exhibited the highest diversity (9.71 ± 2.04), MES E0b showed intermediate values (8.43 ± 0.35), and MES E1–E3 were largely comparable with lower diversity (MES E1: 7.11 ± 0.36; MES E2: 7.14 ± 0.33; MES E3: 7.23 ± 0.32), as summarized in Supplementary Material. Linear modeling, including log-transformed sequencing depth as a covariate, confirmed that group had a significant effect on Shannon diversity (ANOVA: $F = 23.43$, $p = 0.00195$), whereas sequencing depth did not significantly influence the results ($F = 5.90$, $p = 0.059$). Pairwise comparisons further highlighted that OFMSW differed significantly from all MES groups, and MES E0b had moderately higher diversity than MES E2 and E3. Beta diversity analysis revealed marked differences in community composition among groups (Fig. 6b). Bray-Curtis dissimilarity and PCoA showed that OFMSW and MES E0b formed distinct clusters, while MES E1–E3 clustered closely together. PERMANOVA confirmed a significant effect of experimental group on community structure ($R^2 = 0.709$, $p = 0.002$), indicating that the treatments strongly shaped microbial assemblages. Overall, these results demonstrate that the original inoculum harbors a highly diverse microbial community, MES E0b represents an intermediate state, and the remaining MES groups share a similar, treatment-influenced composition. A Linear Discriminant Analysis Effect Size (LEfSe) was run (data not shown), whose results did not add incremental information compared to the strong differences that were already evident from Fig. 5.

The presence of Clostridiaceae and Eubacteriaceae is consistent with their acetogenic/fermentative metabolisms, which are favorable in MES for converting CO_2 (with electron supply) into acetate or other intermediates useful for biomass/protein synthesis (Mateos et al., 2019). Sulfurimonadaceae (and members of the Campylobacterota phylum) may support sulfur or hydrogen metabolism, act as oxygen scavengers, or participate in syntrophic interactions, thus enhancing electron flow or redox balance in cathodic biofilms (K. Zhang et al., 2023). In contrast, communities dominated by Pseudomonadota likely rely more on consuming available organics, rather than efficient carbon fixation or electron use from the electrode. Overall, biochar modifications promote more metabolically versatile and potentially electroactive communities than unmodified electrodes, consistent with boosted MES performance reported for carbonaceous/biochar cathodes (Lekshmi et al., 2023).

4. Outlook on scalability and energy considerations

The present study focused on the laboratory-scale development of biochars with tailored functionalities for MES applications, specifically CO_2 electroreduction.

Although this study was mainly focused on the fabrication and characterization of biochars for electrochemical applications, the scalability and energy demand of the process were considered primary. Regarding the energy consumption of the integrated pyrolysis and activation step, it may be straightforward to treat the process energy consumption separately. Fast pyrolysis of lignocellulosic residual waste

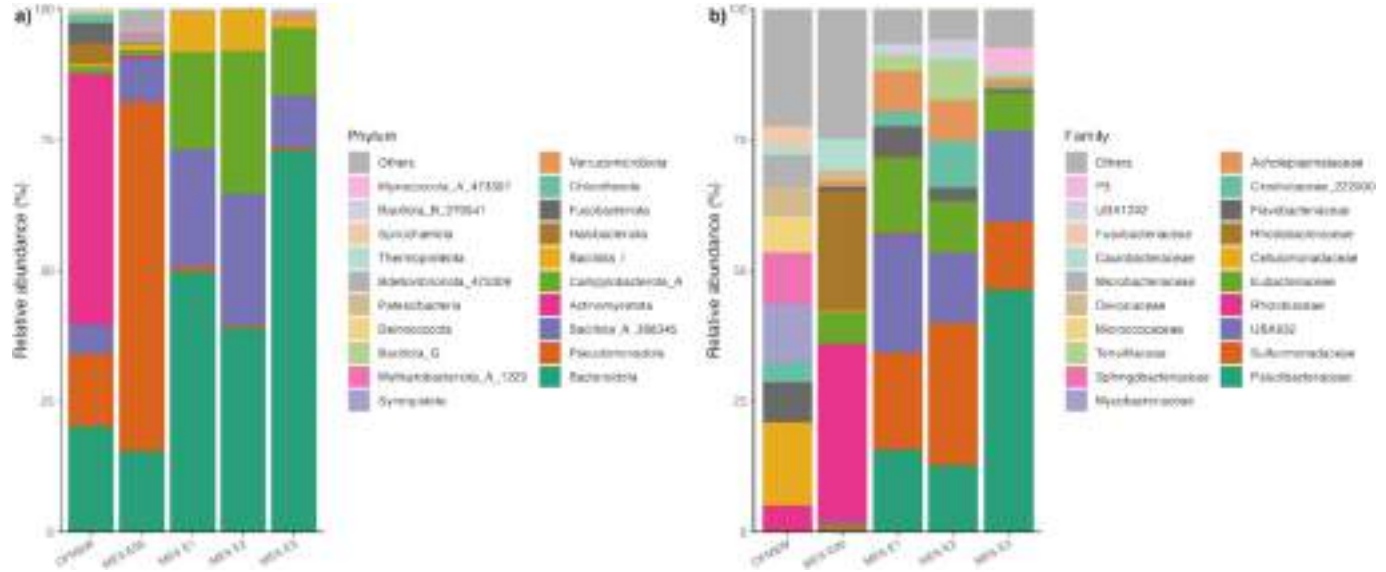

Fig. 5. Relative abundance of the microbial community at the phylum (a) and family (b) levels. Bars represent the mean proportions of the 20 most abundant taxa; all others are grouped as Others.

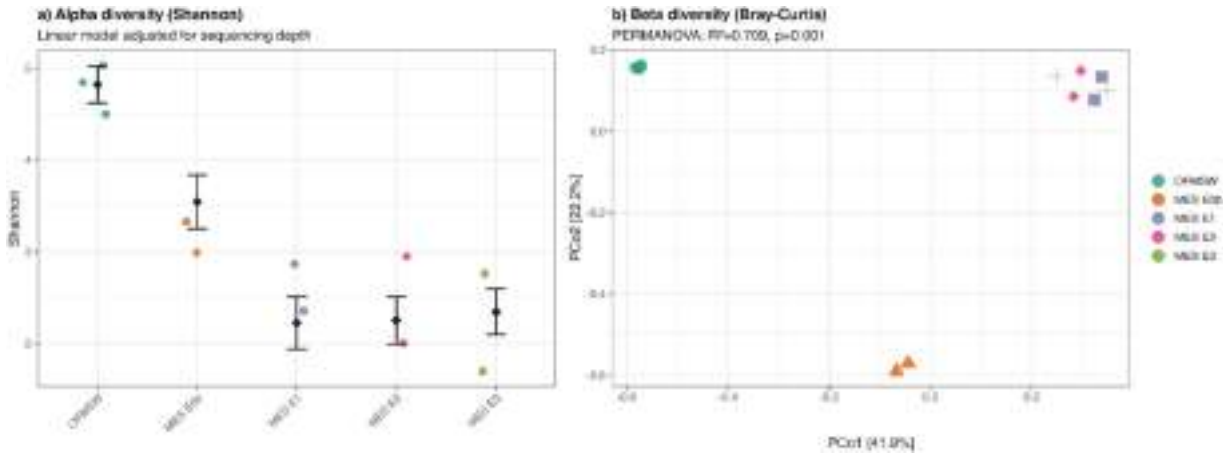

Fig. 6. Microbial diversity in OFMSW and MES experimental groups. (a) Alpha diversity assessed using the Shannon index for the five experimental groups. (b) Beta diversity visualized via Principal Coordinates Analysis (PCoA) based on Bray-Curtis dissimilarity, illustrating differences in microbial community composition among the experimental groups.

is considered a very efficient process, since the enthalpy of reaction is much lower than the high-heating value (HHV) of the raw feedstocks. D. E. Daugaard and R.C. Brown (Daugaard and Brown, 2003) experimentally investigated the enthalpy of pyrolysis of various lignocellulosic biomass, including corn stover, oak and pine residues, and oat hulls, using a bench-scale fluidized-bed reactor in continuous operation. At 500 °C, the enthalpy of pyrolysis, intended as the net heat demand of the process at industrial scale, ranged from 0.8 to 1.6 MJ/kg, representing less than 10 % of the HHV of the various feedstocks. Similarly, our previous investigations evidenced an enthalpy of pyrolysis of 1.59 MJ/kg for the fast pyrolysis of hazelnut shell at 450 °C, performed in a continuous regime using a lab-scale fluidized-bed reactor (Bartolucci et al., 2025). Moreover, the effect of pyrolysis temperature on the energy conversion of hazelnut shells was previously investigated, showing that in the 450–550 °C range the energy yields of the continuous process can be estimated at 72–77 %, in agreement our previous reports (Bartolucci et al., 2024). Hence, it can be concluded that the pyrolytic pre-treatment of biomass is widely recognized as an energy-efficient process. Most previous investigations of the physical activation of biochar under a CO2-rich atmosphere were conducted at the laboratory scale, providing limited information on process scalability and energy demand (Sajjadi et al., 2019). Among the main heterogeneous-phase reactions involved in the physical activation of BC, the Boudouard reaction ($C + CO_2 \rightleftharpoons 2CO$) is considered very relevant. Despite the high endothermicity of the Boudouard reaction, the energy demand of the process can be partly supplied by utilizing cascade waste heat from high-temperature flues. In this perspective, the decentralized biorefinery scheme for biochar production and the centralized activation of biochar appear to be a particularly suitable concept for biochar electrode production from biowaste. The decentralized scheme is particularly suitable for producing value-added products or fuels from fast pyrolysis of lignocellulosic biomass (Fytili and Zabaniotou, 2018; Chiaramonti and Testa, 2024).

Among the principal outcomes of this work, our findings indicate that simpler, one-step synthesis routes may be sufficient for practical applications. In particular, UGW_CO_2_60, obtained via one-step continuous pyrolysis and CO_2 activation without post-functionalization or additional pyrolysis, showed electrochemical performance in MES cells comparable to that of nitrogen-functionalized, multi-step biochars. Although preliminary half-cell tests with rotating disk electrodes suggested improved electrochemical behavior for nitrogen-doped, post-pyrolyzed materials, these differences were largely attenuated once the biochars were integrated into carbon cloth electrodes and operated in MES cells. This attenuation suggests that, for the targeted application, additional functionalization and post-pyrolysis steps do not yield substantial performance gains, despite increased energy consumption and process complexity. From a scalability perspective, this observation is particularly relevant. One-step CO_2 activation routes reduce the number of thermal treatments and intermediate processing steps, thereby lowering overall energy demand and operational complexity. Reported CO_2 activation yields range between 10 and 30 wt%; however, these values were calculated differently depending on the synthesis route. For one-step CO_2-activated biochars, the yield refers to the overall mass relative to the starting biomass, whereas for multi-step nitrogen-doped biochars, it reflects the mass retained after the final processing step. As such, these values are not directly comparable across materials and were not intended to represent CO_2 activation efficiency or process optimization. Nevertheless, the comparatively higher apparent yield and reduced material losses associated with one-step routes further support their suitability for scale-up.

Future efforts toward large-scale implementation should therefore prioritize optimizing one-step pyrolysis/CO_2 activation processes, focusing on parameters such as heating rate, residence time, and CO_2 flow to balance energy consumption, yield, and functional performance. The integration of heat recovery strategies or the use of process-derived energy could further improve the sustainability of biochar production. Overall, the demonstrated adequacy of one-step CO_2-activated biochars in MES cells highlights a viable and scalable pathway for producing functional bioelectrode materials without the need for energy-intensive post-functionalization steps.

5. Conclusions

We developed a carbonization/activation strategy for urban green waste (UGW) feedstock to obtain biochar with maximized nitrogen content, which is inherently present in the feedstock, resulting in the sample UGW_CO_2_60. The effect of further nitrogen enrichment using a nitrogen-rich organic precursor during pyrolysis (UGW(N)_CO_2_60) was then compared, and the impact of an additional pyrolysis step (UGW(N)_CO_2_60_P) on the textural, structural, and electrochemical properties of the resulting biochar was evaluated. Post-treatments led to increased nitrogen content in the biochar, as revealed by elemental analysis, along with enhanced electrochemically active surface area (ECSA) and improved electrocatalytic activity toward ORR in the series: UGW_CO_2_60 < UGW(N)_CO_2_60 < UGW(N)_CO_2_60_P, as demonstrated by rotating disk electrode (RDE) measurements.

The biochars were deposited onto carbon cloth electrodes using an air-spraying technique, thereby optimizing the electrode architecture in terms of both the microporous layer and the catalyst layer. These electrodes were then tested as cathodes in preliminary microbial electrochemical systems (MES) for CO_2 electroreduction. The results showed

higher currents and enhanced electrochemical performance with biochar-modified cathodes, confirming their suitability for bio-electrochemical applications. Microbial analysis of the cathodic biomass further revealed that MES systems with biochar-functionalized electrodes were enriched in the phyla Bacteroidota, Bacillota, and Campylobacterota. In contrast, unmodified electrodes were dominated by Pseudomonadota, supporting the conclusion that biochar modification promotes efficient electron transfer and microbial CO_2 fixation.

CRediT authorship contribution statement

Khair Un Nisa: Writing – original draft, Visualization, Investigation, Data curation. **Beatrice Ricciardi:** Writing – original draft, Visualization, Investigation, Data curation. **Williane da Silva Freitas:** Writing – review & editing, Validation, Supervision, Methodology, Investigation, Conceptualization, Visualization. **Manuela Montalto:** Investigation, Data curation. **Alessandra D'Epifanio:** Writing – review & editing, Supervision, Resources, Methodology, Conceptualization. **Pietro Mele:** Writing – review & editing, Investigation, Data curation. **Lorenzo Bartolucci:** Writing – review & editing, Resources. **Fabrizio Arciprete:** Investigation, Resources, Writing – review & editing. **Gabriele Soggia:** Writing – review & editing, Visualization, Investigation, Data curation. **Fabrizio Adani:** Writing – review & editing, Validation, Resources, Project administration, Funding acquisition, Conceptualization. **Niccolò Forin:** Writing – review & editing, Visualization, Investigation, Data curation. **Andrea Squartini:** Writing – review & editing, Validation, Resources, Conceptualization, Funding acquisition, Project administration. **Barbara Mecheri:** Writing – review & editing, Validation, Supervision, Resources, Project administration, Methodology, Funding acquisition, Conceptualization.

Declaration of competing interest

The authors declare that they have no known competing financial interests or personal relationships that could have appeared to influence the work reported in this paper.

Acknowledgments

This work has received funding from the European Union – Next Generation EU in response to the MUR (Ministry of University and Research) call "PRIN (Project of National Interest) 2022": Project code: 20224WLXRK.

The authors, Lorenzo Bartolucci and Pietro Mele, would like to acknowledge their colleagues, Stefano Cordiner and Vincenzo Mulone, for the opportunity to use the shared facility at the SCERG laboratory of the Tor Vergata University of Rome used for the preparation of the hazelnut shell–derived biochar samples employed in this work, as well as to elemental analysis (CHNS) equipment utilized for material characterization.

Appendix A. Supplementary data

Supplementary data to this article can be found online at https://doi.org/10.1016/j.biortech.2026.134403.

Data availability

Data will be made available on request.

References

Ahmed, K., Hameed, S., Patchigolla, K., Dawood, N., Ghouri, Z.K., 2025. Carbon-based electrocatalysts for hydrogen evolution reaction. Energy Convers. Manage.: X 26, 100892. https://doi.org/10.1016/j.ecmx.2025.100892.

An, H., Park, W., Shin, H., Chung, D.Y., 2024. Recommended practice for measurement and evaluation of oxygen evolution reaction electrocatalysis. EcoMat 6, e12486. https://doi.org/10.1002/eom2.12486.

Antic Gorrazzi, S., Massazza, D., Pedetta, A., Silva, L., Prados, B., Fouga, G., Bonanni, S., 2023. Biochar as a substitute for graphite in microbial electrochemical technologies. RSC Sustainability 1, 1200–1210. https://doi.org/10.1039/d3su00041a.

Artyushkova, K., Serov, A., Rojas-Carbonell, S., Atanassov, P., 2015. Chemistry of multitudinous active sites for oxygen reduction reaction in transition metal–nitrogen–carbon electrocatalysts. J. Phys. Chem. C 119, 25917–25928. https://doi.org/10.1021/acs.jpcc.5b07653.

M. Aysla Costa De Oliveira, A. D'Epifanio, H. Ohnuki, B. Mecheri, Platinum Group Metal-Free Catalysts for Oxygen Reduction Reaction: Applications in Microbial Fuel Cells, Catalysts 2020, Vol. 10, Page 475 10 (2020) 475. https://doi.org/10.3390/CATAL10050475.

Bakonyi, P., Koók, L., Rózsenberszki, T., Kalauz-Simon, V., Bélafi-Bakó, K., Nemestóthy, N., 2023. CO2-refinery through microbial electrosynthesis (MES): a concise review on design, operation, biocatalysts and perspectives. J. CO2 Util. 67, 102348. https://doi.org/10.1016/J.JCOU.2022.102348.

L. Bartolucci, S. Cordiner, G. Kumar, P. Mele, V. Mulone, Intermediate pyrolysis of hazelnut shell: temperature effect on energy conversion and products characteristics, (2024). https://doi.org/10.21203/rs.3.rs-4292816/v1.

Bartolucci, L., Cordiner, S., Mele, P., Mulone, V., 2023. Defatted spent coffee grounds fast pyrolysis polygeneration system: lipid extraction effect on energy yield and products characteristics. Biomass Bioenergy 179, 106974. https://doi.org/10.1016/J.BIOMBIOE.2023.106974.

Bartolucci, L., Cordiner, S., Mele, P., Mulone, V., 2025. Energy efficiency and hydrogen demand of atmospheric fast catalytic hydropyrolysis of residual lignocellulosic biomass. J. Phys. Conf. Ser. 3143, 012005. https://doi.org/10.1088/1742-6596/3143/1/012005.

Bian, B., Bajracharya, S., Xu, J., Pant, D., Saikaly, P.E., 2020. Microbial electrosynthesis from CO2: challenges, opportunities and perspectives in the context of circular bioeconomy. Bioresour. Technol. 302. https://doi.org/10.1016/j.biortech.2020.122863.

Bolyen, E., Rideout, J.R., Dillon, M.R., Bokulich, N.A., Abnet, C.C., Al-Ghalith, G.A., Alexander, H., Alm, E.J., Arumugam, M., Asnicar, F., Bai, Y., Bisanz, J.E., Bittinger, K., Brejnrod, A., Brislawn, C.J., Brown, C.T., Callahan, B.J., Caraballo-Rodríguez, A.M., Chase, J., Cope, E.K., Da Silva, R., Diener, C., Dorrestein, P.C., Douglas, G.M., Durall, D.M., Duvallet, C., Edwardson, C.F., Ernst, M., Estaki, M., Fouquier, J., Gauglitz, J.M., Gibbons, S.M., Gibson, D.L., Gonzalez, A., Gorlick, K., Guo, J., Hillmann, B., Holmes, S., Holste, H., Huttenhower, C., Huttley, G.A., Janssen, S., Jarmusch, A.K., Jiang, L., Kaehler, B.D., Bin Kang, K., Keefe, C.R., Keim, P., Kelley, S.T., Knights, D., Koester, I., Kosciolek, T., Kreps, J., Langille, M.G.I., Lee, J., Ley, R., Liu, Y.X., Loftfield, E., Lozupone, C., Maher, M., Marotz, C., Martin, B.D., McDonald, D., McIver, L.J., Melnik, A.V., Metcalf, J.L., Morgan, S.C., Morton, J.T., Naimey, A.T., Navas-Molina, J.A., Nothias, L.F., Orchanian, S.B., Pearson, T., Peoples, S.L., Petras, D., Preuss, M.L., Pruesse, E., Rasmussen, L.B., Rivers, A., Robeson, M.S., Rosenthal, P., Segata, N., Shaffer, M., Shiffer, A., Sinha, R., Song, S.J., Spear, J.R., Swafford, A.D., Thompson, L.R., Torres, P.J., Trinh, P., Tripathi, A., Turnbaugh, P.J., Ul-Hasan, S., van der Hooft, J.J.J., Vargas, F., Vázquez-Baeza, Y., Vogtmann, E., von Hippel, M., Walters, W., Wan, Y., Wang, M., Warren, J., Weber, K.C., Williamson, C.H.D., Willis, A.D., Xu, Z.Z., Zaneveld, J.R., Zhang, Y., Zhu, Q., Knight, R., Caporaso, J.G., 2019. Reproducible, interactive, scalable and extensible microbiome data science using QIIME 2. Nat. Biotechnol. 37, 852–857. https://doi.org/10.1038/S41587-019-0209-9.

Caizán-Juanarena, L., Borsje, C., Sleutels, T., Yntema, D., Santoro, C., Ieropoulos, I., Soavi, F., ter Heijne, A., 2020. Combination of bioelectrochemical systems and electrochemical capacitors: principles, analysis and opportunities. Biotechnol. Adv. 39, 107456. https://doi.org/10.1016/J.BIOTECHADV.2019.107456.

Calderón, F.J., McCarty, G.W., Reeves, J.B., 2006. Pyrolisis-MS and FT-IR analysis of fresh and decomposed dairy manure. J. Anal. Appl. Pyrol. 76, 14–23. https://doi.org/10.1016/j.jaap.2005.06.009.

Cancelliere, R., Mele, P., Bartolucci, L., Cordiner, S., da Silva Freitas, W., Mazzuca, C., Mecheri, B., Micheli, L., Mulone, V., Paialunga, E., Severini, L., 2025. Mutual interaction of pyrolysis operating conditions and surface morphology for the electrochemical performance of biochar-modified screen-printed electrodes. J. Environ. Chem. Eng. 13, 115477. https://doi.org/10.1016/J.JECE.2025.115477.

Chacón, F.J., Sánchez-Monedero, M.A., Lezama, L., Cayuela, M.L., 2020. Enhancing biochar redox properties through feedstock selection, metal preloading and post-pyrolysis treatments. Chem. Eng. J. 395, 125100. https://doi.org/10.1016/J.CEJ.2020.125100.

Chaudhary, H., Dinakaran, J., Vikram, K., Notup, T., Rao, K.S., 2023. Evaluation of physico-chemical and structural properties of biochar produced from pyrolysis of urban biowaste. J. Mater. Cycles Waste Manag. 25, 2845–2860. https://doi.org/10.1007/S10163-023-01719-3.

Chen, H., Wang, J., Zhang, Z., Zhang, S., 2025. Iron-catalyzed pyrolysis assisted by plastics: a route to highly graphitized porous biochar. J. Anal. Appl. Pyrol. 192, 107328. https://doi.org/10.1016/J.JAAP.2025.107328.

Chen, S., He, Y., Li, Q., Deng, X., Kang, B., He, Y., Lu, Y., Chen, J., Su, C., 2025. Enhancing microbial fuel cell-expanded granular sludge bed for treating sulfate-containing wastewater by adding biochar and hydrochar: performance and potential mechanisms. Bioresour. Technol. 437, 133064. https://doi.org/10.1016/J.BIORTECH.2025.133064.

Chen, W., Qin, Y., Heng, C., Wang, S., Ge, M., Li, Y., Wan, X., Li, X., Shui, J., Su, Y., Su, D., 2025. Degradation of FeNC electrocatalysts for acidic and alkaline oxygen reduction. J. Am. Chem. Soc. 147, 35730–35741. https://doi.org/10.1021/jacs.5c11985.

Chen, W.Q., Foo, J.C.L., Veksha, A., Chan, W.P., Ge, L.Y., Lisak, G., 2024. Unveiling key impact parameters and mechanistic insights towards activated biochar performance for carbon dioxide reduction. Bioresour. Technol. 411, 131355. https://doi.org/10.1016/J.BIORTECH.2024.131355.

Chen, W.Q., Foo, J.L.C., Veksha, A., Chan, W.P., Ge, L.Y., Lisak, G., 2025. Tailoring Cu-loaded activated biochar-based catalysts via N-doping and surfactant modification for tunable C2/CH4 selectivity in CO2 electroreduction. Carbon n. y. 245, 120782. https://doi.org/10.1016/J.CARBON.2025.120782.

Chiaramonti, D., Testa, L., 2024. Deploying EU biomethane potential for transports: centralized/decentralized biogasrefinery schemes to SAF and maritime fuels. Appl. Energy 366. https://doi.org/10.1016/j.apenergy.2024.123306.

Choi, N., Park, C., Lee, S., Cho, K., 2025. Synergistic effects of N-Containing functional groups and calcium binding sites on arsenic adsorption by Ca-N Co-doped microalgae-derived biochar. Sep. Purif. Technol. 379, 134898. https://doi.org/10.1016/J.SEPPUR.2025.134898.

da Silva Freitas, W., Gemma, D., Mecheri, B., D'Epifanio, A., 2022. Air-breathing cathodes for microbial fuel cells based on iron-nitrogen-carbon electrocatalysts. Bioelectrochemistry 146, 108103. https://doi.org/10.1016/J.BIOELECHEM.2022.108103.

Daugaard, D.E., Brown, R.C., 2003. Enthalpy for pyrolysis for several types of biomass. Energy Fuels 17, 934–939. https://doi.org/10.1021/ef020260x.

Ehelebe, K., Schmitt, N., Sievers, G., Jensen, A.W., Hrnjić, A., Collantes Jiménez, P., Kaiser, P., Geuß, M., Ku, Y.P., Jovanovič, P., Mayrhofer, K.J.J., Etzold, B., Hodnik, N., Escudero-Escribano, M., Arenz, M., Cherevko, S., 2022. Benchmarking fuel cell electrocatalysts using gas diffusion electrodes: inter-lab comparison and best practices. ACS Energy Lett. 7, 816–826. https://doi.org/10.1021/ACSENERGYLETT.1C02659.

Escudero-Curiel, S., Díez, A.M., Pazos, M., Sanromán, Á., 2025. Valorized S/N-doped banana peel biochar as a sustainable OER electrocatalyst for green energy applications. IJHE 163, 150728. https://doi.org/10.1016/j.ijhydene.2025.150728.

Feidenhans'l, A.A., Regmi, Y.N., Wei, C., Xia, D., Kibsgaard, J., King, L.A., 2024. Precious metal free hydrogen evolution catalyst design and application. Chem. Rev. 124, 5617–5667. https://doi.org/10.1021/acs.chemrev.3c00712.

Ferrari, A.C., 2007. Raman spectroscopy of graphene and graphite: disorder, electron–phonon coupling, doping and nonadiabatic effects. Solid State Commun. 143, 47–57. https://doi.org/10.1016/J.SSC.2007.03.052.

Ferraro, G., Pecori, G., Rosi, L., Bettucci, L., Fratini, E., Casini, D., Rizzo, A.M., Chiaramonti, D., 2024. Biochar from lab-scale pyrolysis: influence of feedstock and operational temperature. Biomass Convers. Biorefin. 14, 5901–5911. https://doi.org/10.1007/S13399-021-01303-5.

Fu, P., Zhou, L., Sun, L., Huang, B., Yuan, Y., 2017. Nitrogen-doped porous activated carbon derived from cocoon silk as a highly efficient metal-free electrocatalyst for the oxygen reduction reaction. RSC Adv. 7, 13383–13389. https://doi.org/10.1039/C7RA00433H.

Fu, S., Li, M., de Jong, W., Kortlever, R., 2023. Tuning the properties of N-doped biochar for selective CO2 electroreduction to CO. ACS Catal. 13, 10309–10323. https://doi.org/10.1021/ACSCATAL.3C01773.

Fytili, D., Zabaniotou, A., 2018. Circular economy synergistic opportunities of decentralized thermochemical systems for bioenergy and biochar production fueled with agro-industrial wastes with environmental sustainability and social acceptance: a review. Curr. Sustain/renewable Energy Rep. 5, 150–155. https://doi.org/10.1007/s40518-018-0109-5.

Ghodake, G.S., Shinde, S.K., Kadam, A.A., Saratale, R.G., Saratale, G.D., Kumar, M., Palem, R.R., AL-Shwaiman, H.A., Elgorban, A.M., Syed, A., Kim, D.Y., 2021. Review on biomass feedstocks, pyrolysis mechanism and physicochemical properties of biochar: state-of-the-art framework to speed up vision of circular bioeconomy. J. Clean. Prod. 297, 126645. https://doi.org/10.1016/J.JCLEPRO.2021.126645.

Goglio, A., Carrara, A., Elboghdady, H.G.E., Cucina, M., Clagnan, E., Soggia, G., De Nisi, P., Adani, F., 2025. The performance of biochar waste-derived electrodes in different bio-electrochemical applications. J. Power Sources 625, 235623. https://doi.org/10.1016/J.JPOWSOUR.2024.235623.

Guo, S., Peng, J., Li, W., Yang, K., Zhang, L., Zhang, S., Xia, H., 2009. Effects of CO2 activation on porous structures of coconut shell-based activated carbons. Appl. Surf. Sci. 255, 8443–8449. https://doi.org/10.1016/J.APSUSC.2009.05.150.

Hassan, M., Liu, Y., Naidu, R., Parikh, S.J., Du, J., Qi, F., Willett, I.R., 2020. Influences of feedstock sources and pyrolysis temperature on the properties of biochar and functionality as adsorbents: a meta-analysis. Sci. Total Environ. 744, 140714. https://doi.org/10.1016/J.SCITOTENV.2020.140714.

Hassan, S.S., Williams, G.A., Jaiswal, A.K., 2019. Moving towards the second generation of lignocellulosic biorefineries in the EU: drivers, challenges, and opportunities. Renew. Sustain. Energy Rev. 101, 590–599. https://doi.org/10.1016/j.rser.2018.11.041.

Hu, C., Paul, R., Dai, Q., Dai, L., 2021. Carbon-based metal-free electrocatalysts: from oxygen reduction to multifunctional electrocatalysis. Chem. Soc. Rev. 50, 11785–11843. https://doi.org/10.1039/d1cs00219h.

Hu, Y., Jensen, J.O., Bretzler, P., Cleemann, L.N., Yu, J., Li, Q., 2021. Revealing the genuine stability of the reference Pt/C electrocatalyst toward the ORR. Electrochim. Acta 391, 138963. https://doi.org/10.1016/j.electacta.2021.138963.

Huang, H., Reddy, N.G., Huang, X., Chen, P., Wang, P., Zhang, Y., Huang, Y., Lin, P., Garg, A., 2021. Effects of pyrolysis temperature, feedstock type and compaction on water retention of biochar amended soil. Sci. Rep. 11, 1–19. https://doi.org/10.1038/S41598-021-86701-5.

Huang, J., Wang, M., Luo, S., Li, Z., Ge, Y., 2023. In situ preparation of highly graphitized N-doped biochar geopolymer composites for efficient catalytic degradation of tetracycline in water by H2O2. Environ. Res. 219, 115166. https://doi.org/10.1016/J.ENVRES.2022.115166.

Huang, Y., Chen, Y., Xu, M., Asset, T., Tieu, P., Gili, A., Kulkarni, D., De Andrade, V., De Carlo, F., Barnard, H.S., Doran, A., Parkinson, D.Y., Pan, X., Atanassov, P., Zenyuk, I. V., 2021. Catalysts by pyrolysis: direct observation of chemical and morphological transformations leading to transition metal-nitrogen-carbon materials. Mater. Today 47, 53–68. https://doi.org/10.1016/J.MATTOD.2021.02.006.

Imhof, T., Della Bella, R.K.F., Stühmeier, B.M., Gasteiger, H.A., Ledendecker, M., 2023. Towards a realistic prediction of catalyst durability from liquid half-cell tests. PCCP 25, 20533–20545. https://doi.org/10.1039/D3CP02847J.

Janu, R., Mrlik, V., Ribitsch, D., Hofman, J., Sedláček, P., Bielská, L., Soja, G., 2021. Biochar surface functional groups as affected by biomass feedstock, biochar composition and pyrolysis temperature. Carbon Resour. Convers. 4, 36–46. https://doi.org/10.1016/j.crcon.2021.01.003.

Ji, M., Wang, X., Usman, M., Liu, F., Dan, Y., Zhou, L., Campanaro, S., Luo, G., Sang, W., 2022. Effects of different feedstocks-based biochar on soil remediation: a review. Environ. Pollut. 294, 118655. https://doi.org/10.1016/J.ENVPOL.2021.118655.

Jiang, C., Zhang, S., Wang, L., Wu, J., Chen, L., Wang, M., Xiao, Z., Guo, F., Wu, J., Zhang, Y., 2025. Tetracycline adsorption on nitrogen-doped furfural residue biochar: kinetics, thermodynamics and mechanism analysis. Colloids Surf A Physicochem Eng Asp 727, 138197. https://doi.org/10.1016/J.COLSURFA.2025.138197.

Johnravindar, D., Patria, R.D., Lee, J.T.E., Zhang, L., Tong, Y.W., Wang, C.H., Ok, Y.S., Kaur, G., 2021. Syntrophic interactions in anaerobic digestion: how biochar properties affect them? Sustainable Environ. 7. https://doi.org/10.1080/27658511.2021.1945282.

K. Zhang, Y. Deng, Z. Liu, Y. Feng, C. Hu, Z. Wang, Biochar Facilitated Direct Interspecies Electron Transfer in Anaerobic Digestion to Alleviate Antibiotics Inhibition and Enhance Methanogenesis: A Review, International Journal of Environmental Research and Public Health 2023, Vol. 20, Page 2296 20 (2023) 2296. https://doi.org/10.3390/IJERPH20032296.

Keiluweit, M., Nico, P.S., Johnson, M., Kleber, M., 2010. Dynamic molecular structure of plant biomass-derived black carbon (Biochar). Environ. Sci. Technol. 44, 1247–1253. https://doi.org/10.1021/es9031419.

Kumar, K., Dubau, L., Jaouen, F., Maillard, F., 2023. Review on the degradation mechanisms of metal-N-C catalysts for the oxygen reduction reaction in acid electrolyte: current understanding and mitigation approaches. Chem. Rev. 123, 9265–9326. https://doi.org/10.1021/acs.chemrev.2c00685.

Kumar Mishra, R., Jaya Prasanna Kumar, D., Narula, A., Minnat Chistie, S., Ullhas Naik, S., 2023. Production and beneficial impact of biochar for environmental application: a review on types of feedstocks, chemical compositions, operating parameters, techno-economic study, and life cycle assessment. Fuel 343, 127968. https://doi.org/10.1016/J.FUEL.2023.127968.

Lai, Z., Wang, K., Wu, J., Yang, S., Liu, Z., Li, Q., Meng, G., 2025. Removal of imidacloprid by cobalt oxide-activated persulfate anchored on nitrogen-rich biochar: synergistic effect of nitrogen doping and carbon defects. J. Water Process Eng. 77, 108478. https://doi.org/10.1016/J.JWPE.2025.108478.

Langsdorf, A., Halim, M., Volkmar, M., Stöckl, M., Harnisch, R., Hahn, P., Ulber, R., Holtmann, D., 2024. Electrodes from carbonized grass clippings for bioelectrochemical systems. Cleaner Chem. Eng. 9, 100118. https://doi.org/10.1016/j.clce.2024.100118.

Lekshmi, G.S., Bazaka, K., Ramakrishna, S., Kumaravel, V., 2023. Microbial electrosynthesis: carbonaceous electrode materials for CO2 conversion. Mater. Horiz. 10, 292–312. https://doi.org/10.1039/D2MH01178F.

Leng, L., Xiong, Q., Yang, L., Li, H., Zhou, Y., Zhang, W., Jiang, S., Li, H., Huang, H., 2021. An overview on engineering the surface area and porosity of biochar. Sci. Total Environ. 763, 144204. https://doi.org/10.1016/J.SCITOTENV.2020.144204.

Leng, L., Xu, S., Liu, R., Yu, T., Zhuo, X., Leng, S., Xiong, Q., Huang, H., 2020. Nitrogen containing functional groups of biochar: an overview. Bioresour. Technol. 298, 122286. https://doi.org/10.1016/J.BIORTECH.2019.122286.

Li, C., Liu, Y., Luo, M., Cao, J., Fang, F., Feng, Q., Luo, J., Hao, L., Wang, C., 2023. Enhancing simultaneous electrosynthesis of CO2 and nitrogen removal in microbial fuel cell (MFC) cathode compartment by adding Fe–C/biochar compound substrates. J. Power Sources 560, 232707. https://doi.org/10.1016/j.jpowsour.2023.232707.

Li, D., Fu, M., Pei, T., Lu, Y., Liu, C., Lin, X., Hou, D., Sun, H., Luo, C., Zheng, Z., Zheng, Y., 2023. Preparation of nitrogen-containing compounds and nitrogen-doped biochar via nitrogen-rich pyrolysis coupled with ammonia source impregnation. J. Environ. Chem. Eng. 11, 110093. https://doi.org/10.1016/J.JECE.2023.110093.

S. Li, M. Kim, Y.E. Song, S. Hwan Son, H. il Kim, J. Jae, Q. Yan, Q. Fei, J.R. Kim, Housing of electrosynthetic biofilms using a roll-up carbon veil electrode increases CO2 conversion and faradaic efficiency in microbial electrosynthesis cells, Bioresour. Technol. 393 (2024) 130157. https://doi.org/10.1016/J.BIORTECH.2023.130157.

Li, S., Cheng, C., Thomas, A., 2017. Carbon-based microbial-fuel-cell electrodes: from conductive supports to active catalysts. Adv. Mater. 29, 1602547. https://doi.org/10.1002/ADMA.201602547.

Li, S., Ho, S.H., Hua, T., Zhou, Q., Li, F., Tang, J., 2021. Sustainable biochar as an electrocatalysts for the oxygen reduction reaction in microbial fuel cells. Green Energy Environ. 6, 644–659. https://doi.org/10.1016/J.GEE.2020.11.010.

Li, Y., Guan, Y., Zhang, L., 2025. Recent advances in electrochemical applications of sustainable biomass-derived biochar for water purification and soil remediation. Chem. Eng. J. 520, 166340. https://doi.org/10.1016/J.CEJ.2025.166340.

Li, Y., Li, Z., Liu, D., Oksuz, S.T., Li, M., Xu, Q., Chai, F., Liu, P., 2025. Electrode-driven nitrogen conversion in bioelectrochemical systems: mechanisms, advances, and perspectives. J. Water Process Eng. 77, 108613. https://doi.org/10.1016/J.JWPE.2025.108613.

Lian, F., Cui, G., Liu, Z., Duo, L., Zhang, G., Xing, B., 2016. One-step synthesis of a novel N-doped microporous biochar derived from crop straws with high dye adsorption capacity. J. Environ. Manage. 176, 61–68. https://doi.org/10.1016/J.JENVMAN.2016.03.043.

Liu, C., Cui, Y., Li, X., Yao, M., 2021. microeco: an R package for data mining in microbial community ecology. FEMS Microbiol. Ecol. 97, 255. https://doi.org/10.1093/FEMSEC/FIAA255.

Liu, R., Liu, G., Yousaf, B., Abbas, Q., 2018. Operating conditions-induced changes in product yield and characteristics during thermal-conversion of peanut shell to biochar in relation to economic analysis. J. Clean. Prod. 193, 479–490. https://doi.org/10.1016/J.JCLEPRO.2018.05.034.

Liu, X., Zhou, W., Yang, L., Li, L., Zhang, Z., Ke, Y., Chen, S., 2015. Nitrogen and sulfur co-doped porous carbon derived from human hair as highly efficient metal-free electrocatalysts for hydrogen evolution reactions. J. Mater. Chem. A Mater. 3, 8840–8846. https://doi.org/10.1039/C5TA01209K.

R. Mateos, A. Sotres, R.M. Alonso, A. Morán, A. Escapa, Enhanced CO2 Conversion to Acetate through Microbial Electrosynthesis (MES) by Continuous Headspace Gas Recirculation, Energies 2019, Vol. 12, Page 3297 12 (2019) 3297. https://doi.org/10.3390/EN12173297.

McDonald, D., Jiang, Y., Balaban, M., Cantrell, K., Zhu, Q., Gonzalez, A., Morton, J.T., Nicolaou, G., Parks, D.H., Karst, S.M., Albertsen, M., Hugenholtz, P., DeSantis, T., Song, S.J., Bartko, A., Havulinna, A.S., Jousilahti, P., Cheng, S., Inouye, M., Niiranen, T., Jain, M., Salomaa, V., Lahti, L., Mirarab, S., Knight, R., 2024. Greengenes2 unifies microbial data in a single reference tree. Nat. Biotechnol. 42, 715–718. https://doi.org/10.1038/S41587-023-01845-1.

Mecheri, B., Ficca, V.C.A., Costa de Oliveira, M.A., D'Epifanio, A., Placidi, E., Arciprete, F., Licoccia, S., 2018. Facile synthesis of graphene-phthalocyanine composites as oxygen reduction electrocatalysts in microbial fuel cells. Appl Catal B 237, 699–707. https://doi.org/10.1016/J.APCATB.2018.06.031.

A. Mehmood, M. Gong, F. Jaouen, A. Roy, A. Zitolo, A. Khan, M.T. Sougrati, M. Primbs, A.M. Bonastre, D. Fongalland, G. Drazic, P. Strasser, A. Kucernak, High loading of single atomic iron sites in Fe–NC oxygen reduction catalysts for proton exchange membrane fuel cells, Nature Catalysis 2022 5:4 5 (2022) 311–323. https://doi.org/10.1038/s41929-022-00772-9.

Mosch, H.L.K.S., Akintola, O., Plass, W., Höppener, S., Schubert, U.S., Ignaszak, A., 2016. Specific surface versus electrochemically active area of the carbon/polypyrrole capacitor: correlation of ion dynamics studied by an electrochemical quartz crystal microbalance with BET surface. Langmuir 32, 4440–4449. https://doi.org/10.1021/acs.langmuir.6b00523.

Nagai, T., Ioroi, T., 2025. Evaluation of electrochemically active surface area and activity for oxygen evolution reaction for iridium-oxide catalysts. Int. J. Hydrogen Energy 164, 150875. https://doi.org/10.1016/j.ijhydene.2025.150875.

Naik, S.P., Sarkar, O., Gokuladoss, V., Matsakas, L., Mohanakrishna, G., 2025. Role of cathode materials and their advancement for sustainable hydrogen evolution reaction in microbial electrolysis cells. Curr. Opin. Chem. Eng. 49, 101176. https://doi.org/10.1016/j.coche.2025.101176.

Nisa, K.U., da Silva Freitas, W., D'Epifanio, A., Mecheri, B., 2024. Design and optimization of critical-raw-material-free electrodes towards the performance enhancement of microbial fuel cells. Catalysts 14, 385. https://doi.org/10.3390/CATAL14060385.

Nisa, K.U., da Silva Freitas, W., Montero, J., D'Epifanio, A., Mecheri, B., 2023. Development and optimization of air-electrodes for rechargeable Zn–air batteries. Catalysts 13, 1319. https://doi.org/10.3390/CATAL13101319.

Palanisamy, G., Jung, H.Y., Sadhasivam, T., Kurkuri, M.D., Kim, S.C., Roh, S.H., 2019. A comprehensive review on microbial fuel cell technologies: processes, utilization, and advanced developments in electrodes and membranes. J. Clean. Prod. 221, 598–621. https://doi.org/10.1016/J.JCLEPRO.2019.02.172.

Panwar, N.L., Pawar, A., 2022. Influence of activation conditions on the physicochemical properties of activated biochar: a review. Biomass Convers. Biorefin. 12, 925–947. https://doi.org/10.1007/S13399-020-00870-3.

Pardo Pérez, L.C., Sahraie, N.R., Melke, J., Elsässer, P., Teschner, D., Huang, X., Kraehnert, R., White, R.J., Enthaler, S., Strasser, P., Fischer, A., 2018. Polyformamidine-derived non-noble metal electrocatalysts for efficient oxygen reduction reaction. Adv. Funct. Mater. 28, 1707551. https://doi.org/10.1002/adfm.201707551.

Park, S.G., Rhee, C., Jadhav, D.A., Jang, J.H., Hwang, M.H., Chae, K.J., 2025. Enhanced hydrogen production in microbial electrolysis cells through a magnetically induced electroactive anode biofilm. Chem. Eng. J. 505, 159071. https://doi.org/10.1016/j.cej.2024.159071.

Parsa, S.M., Chen, Z., Feng, S., Yang, Y., Luo, L., Ngo, H.H., Wei, W., Ni, B.J., Guo, W., 2025. Metal-free nitrogen-doped carbon-based electrocatalysts for oxygen reduction reaction in microbial fuel cells: advances, challenges, and future directions. Nano Energy 134, 110537. https://doi.org/10.1016/j.nanoen.2024.110537.

Patil, S.A., Arends, J.B.A., Vanwonterghem, I., Van Meerbergen, J., Guo, K., Tyson, G.W., Rabaey, K., 2015. Selective enrichment establishes a stable performing community for microbial electrosynthesis of acetate from CO2. Environ. Sci. Technol. 49, 8833–8843. https://doi.org/10.1021/ES506149D.

Patra, B.R., Mukherjee, A., Nanda, S., Dalai, A.K., 2021. Biochar production, activation and adsorptive applications: a review. Environ. Chem. Lett. 19, 2237–2259. https://doi.org/10.1007/S10311-020-01165-9.

Pepè Sciarria, T., de Oliveira, M.A.C., Mecheri, B., D'Epifanio, A., Goldfarb, J.L., Adani, F., 2020. Metal-free activated biochar as an oxygen reduction reaction catalyst in single chamber microbial fuel cells. J. Power Sources 462, 228183. https://doi.org/10.1016/J.JPOWSOUR.2020.228183.

Q. Jia, W. Liang, M.K. Bates, P. Mani, W. Lee, S. Mukerjee, Activity Descriptor Identification for Oxygen Reduction on Platinum-Based Bimetallic Nanoparticles: In Situ Observation of the Linear Composition–Strain–Activity Relationship, ACS Nano 9 (2015) 387–400. https://doi.org/10.1021/nn506721f.

Qu, X., Han, Y., Chen, Y., Lin, J., Li, G., Yang, J., Jiang, Y., Sun, S., 2021. Stepwise pyrolysis treatment as an efficient strategy to enhance the stability performance of Fe-NX/C electrocatalyst towards oxygen reduction reaction and proton exchange membrane fuel cell. Appl Catal B 295. https://doi.org/10.1016/j.apcatb.2021.120311.

Ramaswamy, N., Mukerjee, S., 2011. Influence of inner- and outer-sphere electron transfer mechanisms during electrocatalysis of oxygen reduction in alkaline media. J. Phys. Chem. C 115, 18015–18026. https://doi.org/10.1021/jp204680p.

Ramírez, Á., Muñoz-Morales, M., López-Fernández, E., Fernández-Morales, F.J., Llanos, J., 2024. Advancing circular economy: critical insights into waste biomass derived carbon electrodes for (bio)electrochemical water treatment. Curr. Opin. Electrochem. 46, 101492. https://doi.org/10.1016/J.COELEC.2024.101492.

Raveendran, A., Chandran, M., Dhanusuraman, R., 2023. A comprehensive review on the electrochemical parameters and recent material development of electrochemical water splitting electrocatalysts. RSC Adv. 13, 3843–3876. https://doi.org/10.1039/d2ra07642j.

Rinaldi, A., Mecheri, B., Garavaglia, V., Licoccia, S., Di Nardo, P., Traversa, E., 2008. Engineering materials and biology to boost performance of microbial fuel cells: a critical review. Energy Environ. Sci. 1, 417–429. https://doi.org/10.1039/B806498A.

Rojas-Carbonell, S., Artyushkova, K., Serov, A., Santoro, C., Matanovic, I., Atanassov, P., 2018. Effect of pH on the activity of platinum group metal-free catalysts in oxygen reduction reaction. ACS Catal. 8, 3041–3053. https://doi.org/10.1021/acscatal.7b03991.

Ruan, G., Yang, Y., Peng, X., Wang, J., Guo, Y., Hu, W., Lin, D., 2025. A review of the current status of nitrogen self-doped biochar applications. J. Environ. Chem. Eng. 13, 115291. https://doi.org/10.1016/J.JECE.2024.115291.

S. Dongre S, G. Zuccante, M. Muhyuddin, C. Lo Vecchio, V. Baglio, E. Berretti, A. Lavacchi, S. R, R.G. Balakrishna, C. Santoro, Innovative biochar-based electrocatalysts from chilli plants and fruits for sustainable oxygen reduction and hydrogen evolution reactions, Electrochim. Acta 517 (2025) 145763. https://doi.org/10.1016/J.ELECTACTA.2025.145763.

Saisuwan, W., Sonsuphab, K., Jenjaiwit, S., Charanaipayuk, N., Ngernyen, Y., Mhuantong, W., Ratpukdi, T., Siripattanakul-Ratpukdi, S., 2025. Triclocarban removal in agricultural runoff using biochar-microbe-augmented bioretention drainage systems: performance and role of microbial community. Bioresour. Technol. 435, 132875. https://doi.org/10.1016/J.BIORTECH.2025.132875.

Sajjadi, B., Chen, W.Y., Egiebor, N.O., 2019. A comprehensive review on physical activation of biochar for energy and environmental applications. Rev. Chem. Eng. 35, 735–776. https://doi.org/10.1515/REVCE-2017-0113.

Samanta, S., Pradhan, A., 2025. Metal-free carbon-based porous materials, promising electrocatalysts for hydrogen fuel production. Chem. Commun. 61, 8108–8119. https://doi.org/10.1039/d5cc01359c.

Sangprasert, T., Sattayarut, V., Rajrujithong, C., Khanchaitit, P., Khemthong, P., Chanthad, C., Grisdanurak, N., 2022. Making use of the inherent nitrogen content of spent coffee grounds to create nanostructured activated carbon for supercapacitor and lithium-ion battery applications. Diam. Relat. Mater. 127, 109164. https://doi.org/10.1016/J.DIAMOND.2022.109164.

Santoro, C., Bollella, P., Erable, B., Atanassov, P., Pant, D., 2022. Oxygen reduction reaction electrocatalysis in neutral media for bioelectrochemical systems. Nat. Catal. 5, 473–484. https://doi.org/10.1038/S41929-022-00787-2.

Santoro, C., Serov, A., Artyushkova, K., Atanassov, P., 2020. Platinum group metal-free oxygen reduction electrocatalysts used in neutral electrolytes for bioelectrochemical reactor applications. Curr. Opin. Electrochem. 23, 106–113. https://doi.org/10.1016/J.COELEC.2020.06.003.

Schmies, H., Bengen, N., Müller-Hülstede, J., Ibitowa, O.A., Wagner, P., Wark, M., 2023. How effective is graphitization of biomasses for the carbon stability of Pt/C ORR catalysts? Catalysts 13, 343. https://doi.org/10.3390/CATAL13020343.

Singh, H., Northup, B.K., Rice, C.W., Prasad, P.V.V., 2022. Biochar applications influence soil physical and chemical properties, microbial diversity, and crop productivity: a meta-analysis. Biochar 4, 1–17. https://doi.org/10.1007/S42773-022-00138-1.

Soggia, G., Goglio, A., Cristiani, P., Luciani, I., Clagnan, E., Adani, F., 2024. Bioelectrochemical protein production valorising NH3-rich pig manure-derived wastewater and CO2 from anaerobic digestion. Renew. Energy 229, 120761. https://doi.org/10.1016/j.renene.2024.120761.

Tan, S., Wang, R., Dong, J., Zhang, K., Zhao, Z., Yin, Q., Liu, J., Yang, W., Cheng, J., 2025. Hydrothermal-mediated in-situ nitrogen doping to prepare biochar for enhancing oxygen reduction reactions in microbial fuel cells. Bioresour. Technol. 416, 131789. https://doi.org/10.1016/J.BIORTECH.2024.131789.

Trasatti, S., Petrii, O.A., 1992. Real surface area measurements in electrochemistry. J. Electroanal. Chem. 327, 353–376. https://doi.org/10.1016/0022-0728(92)80162-W.

Venkatachalam, C.D., Sekar, S., Sengottian, M., Ravichandran, S.R., Bhuvaneshwaran, P., 2023. A critical review of the production, activation, and morphological characteristic study on functionalized biochar. J. Energy Storage 67, 107525. https://doi.org/10.1016/J.EST.2023.107525.

W. da S. Freitas, A. D'Epifanio, V.C.A. Ficca, E. Placidi, F. Arciprete, B. Mecheri, Tailoring active sites of iron-nitrogen-carbon catalysts for oxygen reduction in alkaline environment: Effect of nitrogen-based organic precursor and pyrolysis atmosphere, Electrochim. Acta 391 (2021) 138899. https://doi.org/10.1016/J.ELECTACTA.2021.138899.

Wang, K., Gong, X., Ye, X., Li, J., Yang, Y., Zhu, H., Wang, Y., Yan, L., Zhou, Y., 2024. Dielectric gene engineering on biochar for ultrawide-band microwave absorption with a rational double-layer design. Carbon n. y. 228, 119326. https://doi.org/10.1016/J.CARBON.2024.119326.

Wang, L., Zhu, D., Chen, J., Chen, Y., Chen, W., 2017. Enhanced adsorption of aromatic chemicals on boron and nitrogen co-doped single-walled carbon nanotubes, Environ. Sci. Nano 4, 558–564. https://doi.org/10.1039/C6EN00590J.

Wang, R., Chen, J., Chen, H., 2024. Performance and mechanism of antibiotic resistance removal by biochar-enhanced sediment microbial fuel cell. Bioresour. Technol. 412, 131371. https://doi.org/10.1016/J.BIORTECH.2024.131371.

Wang, Y., Liu, Z., Chen, X., Sun, D., Sun, Y., Liu, L., Li, J., Li, S., 2025. Preparation of biomass activated carbon and its adsorption performance for anionic/cationic dyes (10mg/L): a case study of coffee grounds, hemp stalks and macadamia nut shells. Next Materials 9, 101258. https://doi.org/10.1016/J.NXMATE.2025.101258.

Xie, X., Li, B., Xu, P., Sougrati, M.T., Garcia-Serres, R., Cullen, D.A., Kropf, A.J., Xia, F., Song, M., Saha, S., Zeng, Y., Engelhard, M.H., Bowden, M.E., Zhang, H., Yan, L., Lemmon, T., Li, X.S., Martinez, U., Cheng, Y., Wu, G., Zelenay, P., Ramani, V., Myers, D.J., Jaouen, F., Yang, L., Wang, G., Shao, Y., 2025. Unravelling the stability stressors of atomically dispersed Fe–N–C oxygen reduction catalysts. J. Am. Chem. Soc. 147, 48117–48126. https://doi.org/10.1021/jacs.5c15451.

Xue, C.F., Wang, L., Yang, L.X., Li, J., Li, X.H., Hao, X.G., 2024. Nitrogen self-doped biochar sustainably self-activated from cactus solidified with freeze-drying strategy for lightweight supercapacitor. ACS Sustain. Chem. Eng. 12, 15961–15971. https://doi.org/10.1021/ACSSUSCHEMENG.4C04451.

Xue, Y., Wang, Z., Miao, S., Liu, P., Chen, W., Li, K., 2025. Enhancing capacitive performance through solvent-coupled two-step carbonization of cotton stalk biochar with tunable melamine doping: deciphering the redox activity of pyrrolic nitrogen. Int. J. Hydrogen Energy 106, 1480–1490. https://doi.org/10.1016/J.IJHYDENE.2025.02.057.

Yameen, M.Z., Naqvi, S.R., Juchelková, D., Khan, M.N.A., 2024. Harnessing the power of functionalized biochar: progress, challenges, and future perspectives in energy, water treatment, and environmental sustainability. Biochar 6, 1–80. https://doi.org/10.1007/S42773-024-00316-3.

Yan, X., Jia, Y., Odedairo, T., Zhao, X., Jin, Z., Zhu, Z., Yao, X., 2016. Activated carbon becomes active for oxygen reduction and hydrogen evolution reactions. Chem. Commun. 52, 8156–8159. https://doi.org/10.1039/C6CC03687B.

Yao, S., Zhang, Z., Wang, Y., Liu, Z., Li, Z., 2021. Simple one-pot strategy for converting biowaste into valuable graphitized hierarchically porous biochar for high-efficiency capacitive storage. J. Energy Storage 44, 103259. https://doi.org/10.1016/J.EST.2021.103259.

Yu, H., Zhang, J., Zhai, R., Gao, C., Zhang, Y., Tian, C., Ma, Q., 2024. Magnetic biochar-doped g-C3N4/Fe2O3 S-scheme heterojunction with enhanced photocatalytic degradation of tetracycline by addition of persulfate. Carbon n. y. 230, 119681. https://doi.org/10.1016/J.CARBON.2024.119681.

Zago, S., Scarpetta-Pizo, L.C., Zagal, J.H., Specchia, S., 2024. PGM-free biomass-derived electrocatalysts for oxygen reduction in energy conversion devices: promising materials. Electrochem. Energy Rev. 7, 1–52. https://doi.org/10.1007/S41918-023-00197-3.

Zhang, C., Ji, Y., Li, C., Zhang, Y., Sun, S., Xu, Y., Jiang, L., Wu, C., 2023. The application of biochar for CO2 capture: influence of biochar preparation and CO2 capture reactors. Ind. Eng. Chem. Res. 62, 17168–17181. https://doi.org/10.1021/ACS.IECR.3C00445.

Zhang, C., Ndayisenga, F., Wang, C., Yu, Z., 2025. Electronic configuration of carbon regulated by Mo2C clusters encapsulated in nitrogen self-doped biochar for efficient hydrogen evolution reaction. Chem. Eng. J. 505, 159709. https://doi.org/10.1016/J.CEJ.2025.159709.

Zhang, F., Miao, J., Liu, W., Xu, D., Li, X., 2019. Heteroatom embedded graphene-like structure anchored on porous biochar as efficient metal-free catalyst for ORR. Int. J. Hydrogen Energy 44, 30986–30998. https://doi.org/10.1016/J.IJHYDENE.2019.09.239.

Zhang, H., Sun, L., Luo, S., Yuan, R., Hou, R., Zhou, B., Chen, H., 2025. Electrode materials for copper removal from wastewater by bioelectrochemical systems: a review. J. Environ. Chem. Eng. 13, 116148. https://doi.org/10.1016/J.JECE.2025.116148.

Zhang, W., Xu, D., Zhao, Y., Gao, D., Xie, Z., Zhang, X., Wu, B., Huang, T., Peng, L., 2025. Enhancing electricity generation and pollutant degradation in microbial fuel cells using cyanobacteria-derived biochar electrodes. Bioresour. Technol. 418, 132000. https://doi.org/10.1016/J.BIORTECH.2024.132000.

Zhang, Y., Deng, L., Hu, H., Qiao, Y., Yuan, H., Chen, D., Chang, M., Wei, H., 2020. Pomelo peel-derived, N-doped biochar microspheres as an efficient and durable metal-free ORR catalyst in microbial fuel cells. Sustain Energy Fuels 4, 1642–1653. https://doi.org/10.1039/C9SE00834A.

Zhao, C., Liu, X., Chen, A., Chen, J., Lv, W., Liu, X., 2024. Characteristics evaluation of bio-char produced by pyrolysis from waste hazelnut shell at various temperatures. Energy Sources Part A 46, 7403–7413. https://doi.org/10.1080/15567036.2020.1754530.

Zheng, X., Xie, J., Chen, W., Liu, M., Xie, L., 2024. Boosting anaerobic digestion of long chain fatty acid with microbial electrolysis cell combining metal organic framework as cathode: biofilm construction and metabolic pathways. Bioresour. Technol. 395, 130284. https://doi.org/10.1016/J.BIORTECH.2023.130284.

Zhong, K., Li, M., Yang, Y., Zhang, H., Zhang, B., Tang, J., Yan, J., Su, M., Yang, Z., 2019. Nitrogen-doped biochar derived from watermelon rind as oxygen reduction catalyst in air cathode microbial fuel cells. Appl. Energy 242, 516–525. https://doi.org/10.1016/J.APENERGY.2019.03.050.

Zitolo, A., Goellner, V., Armel, V., Sougrati, M.T., Mineva, T., Stievano, L., Fonda, E., Jaouen, F., 2015. Identification of catalytic sites for oxygen reduction in iron- and nitrogen-doped graphene materials. Nat. Mater. 14, 937–942. https://doi.org/10.1038/nmat4367.